

Strained Si, Ge, and $\text{Si}_{1-x}\text{Ge}_x$ alloys modeled with a first-principles-optimized full-zone $k\cdot p$ method

D. Rideau,* M. Feraille,† L. Ciampolini, M. Minondo, C. Tavernier, and H. Jaouen
STMicroelectronics, rue Jean Monnet, 850, BP 16, F-38926 Crolles Cedex, France

A. Ghetti

STMicroelectronics, via C. Olivetti, 2, I-20041 Agrate Brianza, Italy

(Received 20 July 2006; revised manuscript received 9 October 2006; published 28 November 2006)

The electronic energy band structure of strained and unstrained Si, Ge, and SiGe alloys is examined in this work using a 30-level $k\cdot p$ analysis. The energy bands are at first obtained with *ab initio* calculations based on the local-density approximation of density-functional theory, including a *GW* correction and relativistic effects. The so-calculated band structure is then used to extract the unknown $k\cdot p$ fitting parameters with a conjugate-gradient optimization procedure. In a similar manner, the results of *ab initio* calculations for strained materials are used to fit the unknown deformation potentials that are included in the present $k\cdot p$ Hamiltonian following the Pikus-Bir correction scheme. We show that the present $k\cdot p$ model is an efficient numerical method, as far as computational time is concerned, which reproduces accurately the overall band structure, as well as the bulk effective density of states and the carrier effective masses, for both strained and unstrained materials. As an application, the present 30-level $k\cdot p$ model is used to describe the band offsets and the variations of the carrier effective masses in the strained $\text{Si}_{1-x}\text{Ge}_x/\text{Si}_{1-y}\text{Ge}_y$ system.

DOI: [10.1103/PhysRevB.74.195208](https://doi.org/10.1103/PhysRevB.74.195208)

PACS number(s): 71.15.Mb, 71.20.Nr

I. INTRODUCTION

The continuous downscaling of metal-oxide-semiconductor field-effect-transistor (MOSFET) critical dimensions such as the gate length and gate oxide thickness has been a very successful trend in current manufacturing, as testified, e.g., by the ITRS requirements. However, conventional scaling down of the MOSFET channel length is declining as the physical and economic limits of such an approach are coming closer. Novel solutions are increasingly being used in MOSFET channel engineering. The growth of a strained Si layer on a relaxed $\text{Si}_{1-y}\text{Ge}_y$ buffer layer is a typical technique used to improve the electrical performances of MOSFET devices, due to the expected enhancements in the carrier mobility^{1,2} of such a strained layer. High-performance strained $\text{Si}_{1-x}\text{Ge}_x$ transistors have been recently obtained, and this technology could feature in the future chip generation with channel size of 32 nm or less.^{1,3} When modeling the electrical currents of such devices, it is required to take into account the fundamental carrier transport properties that are governed by the structure of the electronic energy bands of the strained material.

Material science computational methods for the calculation of the electronic energy band structure fall into two general categories. The first category includes the *ab initio* methods, such as Hartree-Fock or density-functional theory (DFT), which calculate the electronic structure from first principles—i.e., without the need for empirical parameters. The second category consists of far more computationally efficient semiempirical methods such as the empirical pseudopotential method (EPM), the tight binding (TB) method, and the $k\cdot p$ method.

Over the past decades, the local-density approximation (LDA) variant of DFT (Ref. 4) has been established as a very powerful tool for studying the elastic properties and the de-

formation potentials of strained semiconductors.^{5–8} More recently, the *GW* many-body correction to the LDA DFT (Ref. 9) has yielded semiconductor band structures that feature band gap values near their experimental values. *Ab initio* methods are self-consistent methods which utilize a variational approach to calculate the ground-state energy of a many-body system and thus require large computer resources. They can only be used in particular situations of high symmetries and are not suitable for calculating the transport properties of large systems with confined edge states.

Unlike *ab initio* approaches, EPM, TB, and the $k\cdot p$ method involve fitting parameters to reproduce the experimental energy band gaps, the dielectric response, and the carrier effective masses. Over the past three decades, the EPM with spin-orbit (SO) corrections has proven to be extremely successful in calculating the electronic band structure of relaxed and strained semiconductors with indirect gap.^{10–14} Recent calculations using the TB method have also given accurate results.^{15,16} In the $k\cdot p$ method, the energy band structure is obtained by a set of parameters which represent the energy gaps at Γ , the momentum matrix elements, and the strength of the SO coupling. The number of energy bands (or levels) that are effectively calculated is related to the precision of the results. The six-level $k\cdot p$ model,¹⁷ eight-level $k\cdot p$ model, and 14-level $k\cdot p$ model¹⁸ give an accurate description of the highest valence bands (VBs) and the lowest conduction bands (CBs) of semiconductors near the center Γ of the Brillouin zone, but fail to describe the CBs of semiconductors with an indirect gap. Low-order $k\cdot p$ Hamiltonians need a small number of parameters (typically less than 10), while high-order $k\cdot p$ methods,¹⁹ referred to by Pollak *et al.*²⁰ as “full-zone” $k\cdot p$ methods, require a large number of unknown parameters. While it is a straightforward matter to work out the energy band structure at any k point in

the Brillouin zone, once these parameters have been chosen, it requires effort and skill to come up with a satisfactory set of parameters.²⁰ For this reason, the full-zone $k \cdot p$ method has been used rarely and for a few *bulk* semiconductors only, including Si, Ge,^{19,21,22} and α -Sn,²⁰ while no extensive calculations have been published for strained semiconductors.

In this paper, we propose to extend to strained Si, Ge, and SiGe alloys the 30-level $k \cdot p$ model that was first introduced by Cardona and Pollock.¹⁹ For the first time, the well-known Pikus-Bir²³ correction for strained materials has been combined within this 30-level $k \cdot p$ formalism. The $k \cdot p$ parameter optimization strategy is based on a conjugate-gradient procedure that uses *ab initio* simulations but also a large amount of experimental data that are currently available for Si and Ge.

In the first part of this paper, a series of *ab initio* DFT-LDA simulations that include the GW correction and relativistic effects in strained $\text{Si}_{1-x}\text{Ge}_x/\text{Si}_{1-y}\text{Ge}_y$ systems has been performed with a view to complete the experimental data and to establish a reference set of energy bands. In the second part of this paper, we have determined the $k \cdot p$ model coupling parameters and the deformation potentials that fit as closely as possible the first-principles results, matching not only the energy levels and the carrier effective masses, but also the general shape of the band structure of relaxed and strained crystals. A simple interpolation between the $k \cdot p$ parameters for Si and those for Ge has been proposed in order to model SiGe alloys. In the third part of this paper, a set of comparisons is given with experimental data in relaxed and strained Si, Ge, and $\text{Si}_{1-x}\text{Ge}_x$ alloys. We show that the present $k \cdot p$ model accurately reproduces the overall band structure, as well as the band shifts and the carrier effective masses versus applied strain. A second set of comparisons with the widely used Chelikowsky-Cohen nonlocal EPM (Ref. 10) has also shown a good agreement with $k \cdot p$ simulations.

II. FIRST-PRINCIPLES SIMULATION SETUP

A. Bulk material

A series of first-principles calculations has been performed in Si and Ge to obtain a reference set of energy bands, which can be used later for the $k \cdot p$ model parameter optimization. The first-principles results presented in this work have been obtained within the LDA variant of the DFT.²⁴ The present DFT-LDA calculation relies on the pseudopotential (PP) approximation, by which the core states are effectively eliminated from the calculation. We have used the Hartwigsen-Goedecker-Hutter relativistic separable dual-space Gaussian PP,²⁵ which uses the Cerperley-Alder exchange-correlation functional.²⁶ These PPs include relativistic effects and provide an accurate description of the VBs in the near Γ region, a critical region with respect to the hole transport properties in semiconductors.

The value of the equilibrium lattice parameter has been calculated by minimizing the total energy. Any further LDA calculation have used this theoretical value, instead of the experimental one,²⁷ yielding thus a consistent set of zero-pressure reference data. In Si, we found $a_0=5.387$ Å and, in

Ge, $a_0=5.585$ Å. These values agree within 0.75% and 1.33% with the experimental values of 5.431 Å and 5.658 Å,²⁸ respectively.

It is known that the band gaps calculated with the LDA method are generally below their experimental values. However, the agreement can be greatly improved by the use of the Hedin's GW correction.⁹ In practice this correction can be applied as a post-DFT scheme²⁹⁻³¹ in a non-self-consistent way. In the following work, the G_0W_0 corrections of bulk Si and Ge were computed on 19 high-symmetry points in the Brillouin zone and added in a perturbative manner to the LDA band structure. One remark deserves notice: In spite of the G_0W_0 correction, the theoretical lowest CBs typically lie within 0.05–0.2 eV of the range of experimental energies observed.²⁹ In the present work, the G_0W_0 theoretical indirect gaps have been found to be 1.076 eV in Si (located at 84% away from Γ along the Γ -X direction) and 0.64 eV in Ge, which is underestimated by 8% and 14%, respectively. Our results compare favorably with other LDA- GW results found in the literature (e.g., see the extensive comparison between first-principles calculations summarized in the review by Aulbur *et al.*²⁹). Even though correctly parametrized, LDA- G_0W_0 results do not match *perfectly* with experimental data, and significant theoretical work such as vertex correction, self-consistent- GW , and the exact treatment of the exchange term are currently in progress to further improve DFT results.²⁹ These alternative approaches are beyond the scope of the present work. For the purpose of obtaining a reference set of energy bands that can be used in the development of an optimized $k \cdot p$ model, we used the non-self-consistent G_0W_0 approximation to correct the band gap problem and we applied a supplementary rigid “scissors” shift of 0.09 eV for Si and 0.104 eV for Ge in order to obtain the final reference set of energy bands, the GW energy levels.³²

Aside from the above studies, the accuracy of the DFT-LDA calculation critically depends on the manner in which the problem is sampled numerically.³³ We found a good LDA convergence ($\Delta E_k \leq 0.01$ eV) using a basis set of approximately 1300–1500 plane waves, which corresponds to a cut-off energy of around 22 hartrees. The Brillouin zone was sampled on a $6 \times 6 \times 6$ fourfold-shifted Monkhorst-Pack (MP) grid³⁴ (i.e., 864 k points) to obtain the charge density. As regards the G_0W_0 correction, a satisfactory trade-off between numerical convergence and computation time was achieved with a cutoff energy of 8 hartrees and using a large number of bands (>100) included in the calculation of the self-energy.³⁵

B. SiGe alloys

In $\text{Si}_{1-x}\text{Ge}_x$, where x denotes the relative mole fraction of the two materials, both Si and Ge atoms are present in the unit cell. For this reason, we used a 32-atom tetragonal cell sampled on a $(4 \times 4 \times 2)$ -shifted MP grid to simulate $\text{Si}_{1-x}\text{Ge}_x$ alloys when $x \neq \{0; 0.5; 1\}$. The Si and Ge atoms have been randomly distributed in the supercell, and a structural optimization of the atomic positions in the unit cell has been performed. A linear interpolation between the GW cor-

TABLE I. Eigenvalues and SO splittings of Γ -centered states. Symbols of Ref. 19. The $\Gamma_{25'1}$ eigenvalue is arbitrarily set to zero. Δ symbols refer to the state's SO splittings. All energies are expressed in eV.

States at Γ	Si			Ge			Si _{1-x} Ge _x $k \cdot p^e$
	Expt.	EPM ^a	$G_0W_0^a$	Expt.	EPM ^a	$G_0W_0^a$	
$\Gamma_{1'}$	-12.4±0.6, ^b -11.2, ⁱ -12.5±0.6, ^c -11.4 ⁱ	-12.36	-11.489	-12.6±0.3 ^b , -12.9±0.2 ^h	-12.624	-12.638	-12.7-0.18x
$\Delta_{25'1}$	0.044 ^c	0.044	0.0499	0.296 ^c	0.297	0.312	0.044+0.2x+0.052x ²
Γ_{15}	3.4, ^c 3.35, ^f 3.05 ^d	3.406	3.204	3.006, ⁱ 3.206, ⁱ 3.16, ^g 3.25, ^c	3.279	3.1	3.335-0.222x
Δ_{15}	0.04 ^c	0.037	0.037	0.200 ^e	0.205	0.227	0.033+0.157x
$\Gamma_{2'1}$	4.15, ⁱ 4.1, ^d 4.185, ^c 4.21 ⁱ	4.062	3.96	0.89, ^h 0.90 ⁱ	0.861	0.715	4.15-3.26x
Γ_{1u}		7.561	8.308		6.072	6.82	8.4-1.6x
$\Gamma_{12'}$		9.371	8.451		8.665	9.925	8.54+1.76x
$\Gamma_{25'u}$		12.203	11.41		11.334	11.193	11.7-0.34x
$\Delta_{25'1u}$		0.009	0.012		0.0558	0.029	0.012+0.03x
$\Gamma_{2'1u}$		13.3	15.41		12.97	14.086	15.8-1.8x

^aPresent calculations.^bAs presented in Ref. 10.^cAs presented in Ref. 28.^dReference 38.^eAs used in the present $k \cdot p$ model.^fReference 40.^gReference 41.^hAs presented in Ref. 42.ⁱAs presented in Ref. 29.

rection of Si and Ge was used to correct the band gap. This latter approximation is reasonable because the GW corrections obtained in Si and Ge are effectively very close.²⁹

The experimental lattice parameter in Si_{1-x}Ge_x is well described by Dismukes's law³⁶ according to which $a^{expt}(x) = 5.431 + 0.2x + 0.027x^2$ is a quadratic function of x . A similar expression has been obtained from our theoretical results at various x contents:

$$a^{theo}(x) = 5.387 + 0.1428x + 0.0532x^2. \quad (1)$$

C. Strained material

A series of first-principles simulations of the electronic band structure has been performed with a view to fitting the deformation potentials needed in the development of the $k \cdot p$ model for strained materials, which is presented in the next section. For this purpose, epitaxial Si_{1-x}Ge_x layers grown on a relaxed Si_{1-y}Ge_y buffer are studied for a large range of biaxial strain (ϵ_{\parallel} up to 4%) applied perpendicularly to the [001], [111], and [110] directions.

As is known, the normal stresses and the inner displacement of atoms in the cell strongly influence the electronic and structural properties of the strained crystal.³⁷ For this reason, the present simulations include a structural optimization of the unit cell of the strained crystal. The calculations are performed as follows.

(i) The longitudinal strain $\epsilon_{\parallel} = a(y)/a_0 - 1$ is calculated from the slight difference between the Si and Ge relaxed lattice parameter a_0 and the Si_{1-y}Ge_y one in the buffer $a(y)$ that is determined from Eq. (1). The shape of the distorted

cell and the position of the atoms in the cell are obtained by minimizing the total energy of the biaxially strained crystal (following the procedure described in Appendix A).

(ii) The optimized cell is used later in the DFT-LDA band structure calculations.

(iii) The GW correction of *bulk* Si and Ge is used to correct the band gap problem. This choice was motivated by the work of Zhu *et al.*³⁸ reporting that there is no quantitative difference in Si between the LDA band gap pressure dependences and the ones from a full GW calculation.

III. DEVELOPMENT OF AN OPTIMIZED $k \cdot p$ MODEL

A. $k \cdot p$ parameters for bulk materials

The $k \cdot p$ formalism using a zinc-blende Γ -centered Bloch function basis $u_{lk}(\mathbf{r}) = \sum_n C_n^l u_{n0}(\mathbf{r})$ leads to the secular $k \cdot p$ equation of the undeformed crystal:¹⁷

$$\sum_n \left\{ \left(\frac{\hbar^2 k^2}{2m} + E_n^0 - E_{lk} \right) \delta_{n,n'} + \frac{\hbar \mathbf{k}}{m} \cdot \langle u_{n'0} | \mathbf{p} | u_{n0} \rangle \right\} C_n^l = 0, \quad (2)$$

where E_n^0 are the eigenvalues at Γ . The 15 Γ states from group O^h determined by Cardona and Pollock¹⁹ (shown in Table I) is our starting point. The number of independent nondiagonal matrix elements in Eq. (2) can be reduced to 10 in Si and Ge using group-theory selection rules.^{19,43} The SO coupling terms are introduced in the usual way,^{17,20} leading to a 30×30 $k \cdot p$ matrix (see Appendix B). We note, incidentally, that since this approach does not use renormalized Luttinger-type parameters, it is different from other lower-

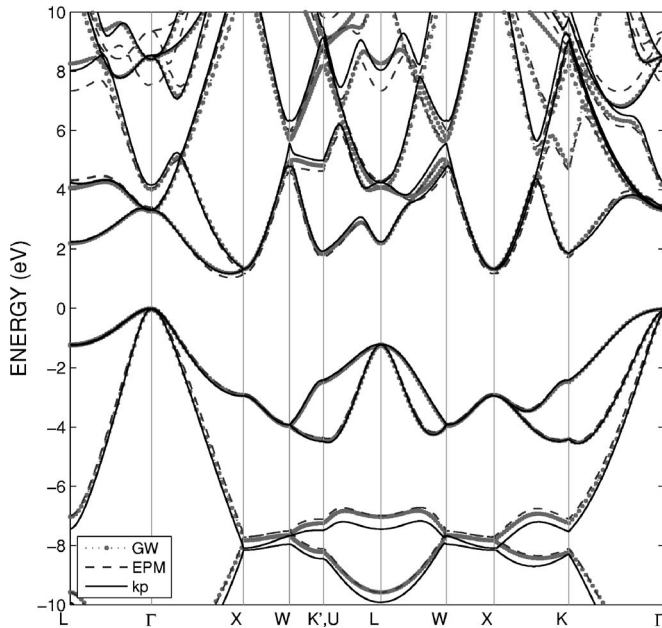


FIG. 1. Bulk Si electronic band structure obtained using the 30-level $k\cdot p$ model, EPM, and GW calculation.

order $k\cdot p$ models such as the 14-level $k\cdot p$ model of Ref. 18 and the 20-level model of Ref. 44.

As written in Appendix B, the 30-level $k\cdot p$ model depends on seven Γ -centered eigenvalues, four SO coupling coefficients, and ten matrix elements. In the development of the present optimized $k\cdot p$ model, we attempted to fit experimental electronic properties of Si, Ge, and SiGe alloys as closely as possible. Currently, there is insufficient detailed experimental information about the band energies to accurately determine all the $k\cdot p$ parameters, particularly at high energy (>5 eV). For this reason, we adopted a mixed approach using experimental data when available and *ab initio* results otherwise. These coefficients were fitted using a conjugate-gradient procedure. Satisfactory convergence was determined through a least-squares error function between $k\cdot p$ eigenvalues and GW results evaluated on a dense (~ 1000) set of k points in the Brillouin zone. Particular care has been given in the near- Γ region and at the CB minima in order to obtain an accurate description of the curvature masses and Luttinger parameters. We also tried as far as possible to reduce the discontinuity in energy at the K - and U -equivalent points.²⁰ Due to missing high-energy (220) bands in the present $k\cdot p$, eigenvalues at K and U differ from several meV (~ 7 meV). The coupling between (220) states to the other 30-lowest-energy states is naturally more pronounced near K , where the lowest (220) eigenvalues are as low as ~ 4.5 eV. For comparison, the lowest (220) eigenvalues are ≥ 26 eV at Γ , ≥ 12.5 eV at X , and ≥ 12 eV at L . After several attempts to remove this discontinuity by changing the $k\cdot p$ parameter values only, we found out that no satisfactory trade-off between accuracy and continuity in K and U could be obtained. For this reason, the present $k\cdot p$ model has a discontinuity in K and U (Ref. 45) (as in Ref. 19).

Following Pollak *et al.*,²⁰ the SO strength between Γ_{25^u} and Γ_{25^l} states was determined by imposing the highest VBs

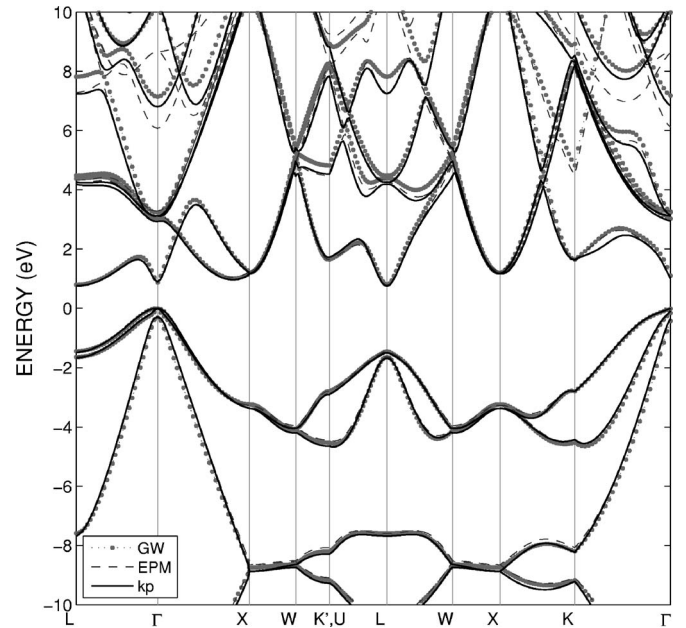


FIG. 2. Bulk Ge electronic band structure obtained using the 30-level $k\cdot p$ model, EPM, and GW calculation.

to be degenerated at X . $\Delta_{25^l} = 44$ meV for Si and $\Delta_{25^l} = 290$ meV for Ge are known by experiments, while Δ_{25^u} and Δ_{15} were obtained from first-principles simulations (see Table I).

The Γ -centered eigenvalues and the coupling parameters obtained from our procedure are listed in Table I and Table V in Appendix A. It ought to be mentioned that there are two sets of published $k\cdot p$ parameters in Si (Refs. 21 and 22) and one set in Ge (Ref. 21) based on the early work of Cardona and Pollak.¹⁹ Although the initial Cardona and Pollak's parameters set¹⁹ provides an accurate description of the main CB minima and the top of the VBs, it has the limitation of not including the SO coupling (due to computational limitations in the mid-60s). This was recently done in Si and Ge (Ref. 21) together with a new set of parameters. Unfortunately in Ge, the proposed set of parameters failed to improve Cardona and Pollak's¹⁹ one in so far as none of the VBs reach the edge of the Brillouin zone with zero slope (or average slope) as required by crystal symmetry and the L -valley minima are very distant from the Brillouin zone edge. This later drawback makes this model inappropriate for application to transport properties in nanostructures. This was not the case with Cardona and Pollak's parameters set,¹⁹ but also with the present one. In comparison to this former set of parameters, our optimization strategy based on an *ab initio* reference set of energy bands brings additional information (notably at high energies) and slightly improves the accuracy of the carrier group velocity at the first and second CB minima, but also certain energy gap values in both Si and Ge. The matrix elements listed in Table V are slightly different from Cardona and Pollak's¹⁹ ones. The main differences⁴⁶ come from the fact that the Γ eigenvalues used in the present $k\cdot p$ model differ at high energy ($E > 3.5$ eV) and that nonlocal effects have been accounted for in the present model.⁴⁷

TABLE II. Deformation potentials (eV).

Si	Expt. ^a	EPM ^b	LDA ^c	$k \cdot p^c$
b_v	-2.10 ± 0.10	-2.12	-2.27	-2.27
d_v	-4.85 ± 0.15	-4.56	-4.36	-4.36
$(\Xi_d^\Delta + \frac{1}{3}\Xi_u^\Delta - a_v)$	1.50 ± 0.30	2.24	1.67	1.94
$(\Xi_d^L + \frac{1}{3}\Xi_u^L - a_v)$		-1.4	-3.14	-3.03
Ξ_u^Δ	8.6 ± 0.4	9	8.79	9.01
Ξ_u^L		15.9	13.85	15.1
Ge	Expt. ^a	EPM ^b	LDA ^c	$k \cdot p^c$
b_v	-2.86 ± 0.15	-2.81	-2.9	-2.8
d_v	-5.28 ± 0.50	-5.31	-6	-5.5
$(\Xi_d^\Delta + \frac{1}{3}\Xi_u^\Delta - a_v)$		3.12	1.43	1.83
$(\Xi_d^L + \frac{1}{3}\Xi_u^L - a_v)$	-2.0 ± 0.5	-2.26	-2.86	-1.97
Ξ_u^Δ		9.91	10	10
Ξ_u^L	16.2 ± 0.4	16.3	17	16.3

^aCited by Ref. 6.^bPresent Chelikowsky-Cohen-based EPM (Refs. 10 and 50).^cPresent work.

The Si and Ge band structures (BSs) obtained using the present $k \cdot p$ parameters set are compared to GW first-principles simulations in Figs. 1 and 2. The overall quality of the fit is excellent: The difference in band energies between our semiempirical values and those used for the fit was typically less than 0.01 eV for the principal band gaps and under 0.3 eV at other high-symmetry points. Further comparisons are shown with the widely used Chelikowsky-Cohen nonlocal EPM.¹⁰ As can be seen, the straightforward application of the EPM yields a BS that is in very good agreement (up to more than 6 eV) with the results of the much more complex GW *ab initio* calculation. This excellent agreement means that both methods are consistent and lends further support to the GW reference set of energy bands used for the $k \cdot p$ parameter optimization.

B. SiGe alloy parameters

The virtual crystal approximation was used to extend the $k \cdot p$ results to SiGe alloys. A quadratic interpolation between Si and Ge parameters is proposed in Tables I and V. Due to centrosymmetry breaking, SiGe alloys do not belong to group O^h . A supplementary SO coupling term⁴⁸ and two purely imaginary coupling terms from group T^d (Ref. 49) (not shown in Appendix B) have been introduced in Table V. These interpolation coefficients were determined in order to fit the GW Si_{1-x}Ge_x band structures for various x -content values (see, e.g., in Fig. 3 the Si_{0.5}Ge_{0.5} band structure obtained with the present $k \cdot p$ parameters interpolated at $x=0.5$). The present $k \cdot p$ model predicts a crossing between Δ -valley and L -valley minima at $x=0.84$ (not shown) which is consistent with the experimental data.¹

C. Strained materials: deformation potentials

The analysis of the structure of strained semiconductors using the $k \cdot p$ Hamiltonian has been initially proposed by

Pikus and Bir.²³ These authors derived the first-order $k \cdot p$ perturbation terms arising from straining the semiconductor in question. This general expression has been widely used in the six-level $k \cdot p$ Hamiltonian to analyze the effect of deformation on the hole energy spectrum. For the first time, we applied the Pikus-Bir formalism in the case of the 30-level $k \cdot p$ Hamiltonian. The perturbation term to be added to Eq. (2) can be written as²³

$$W_{n',n} = - \sum_{i,j} \frac{\hbar}{m} \epsilon_{ij} k_i \langle u_{n'0} | p_j | u_{n0} \rangle + \epsilon_{ij} \langle u_{n'0} | \Xi_{ij} | u_{n0} \rangle, \quad (3)$$

where i, j stand for x, y, z . The first term of Eq. (3), accounts for the interaction between the strain and the momentum of the carriers. The deformation potential operator $\Xi_{ij} = -\frac{p_i p_j}{m} + V_{ij}(\mathbf{r})$ describes the change in the potential and the kinetic energy of carriers due to the strain itself. The unknown non-vanishing deformation potentials at $\Gamma \langle u_{n'0} | \Xi_{ij} | u_{n0} \rangle$, listed in Table VII (Appendix C), were determined from group-theory selection rules, taking into account the $p_i p_j$ contribution only. This choice is motivated by the fact that in the deformed-ion approximation the V_{ij} term with rhombic or tetragonal symmetries vanishes.²³

The perturbation matrix W to be added to the 30 $k \cdot p$ matrix is shown in Appendix C. Accurate knowledge of the deformation potentials at Γ for *all* 30 lowest-energy bands is required for the construction of the $k \cdot p$ model in the strained material. However, only deformation potentials for the $\Gamma_{25'}$ states are known experimentally⁶ in Si and Ge. The deformation potentials, needed in Eq. (3) and listed in Table II, have been fitted using a procedure similar to the one used in bulk materials. We have used a least-squares optimization procedure on GW energy levels calculated for various distorted crystals, including shear distortions. Special attention has been given to the time-reversal symmetry degeneracy at the edge of the Brillouin zone. In addition to space-group sym-

TABLE III. Eigenvalues and energy gaps at high-symmetry points in the Brillouin zone calculated with the EPM, $k \cdot p$ and GW methods (see text for details). The state's SO splittings are shown in parentheses. Averaged values over transitions between SO-split bands are noted with a bar. All energies are in eV.

States ^a	Si				Ge			
	Expt.	EPM	G_0W_0	$k \cdot p$	Expt.	EPM	G_0W_0	$k \cdot p$
L_1	-6.8 ± 0.2^b , -6.4^i -6.7 ± 0.2^d	-6.991	-7.019	-7.448	-7.7 ± 0.2^b	-7.588	-7.801	-7.678
L'_3	-1.5^c , -1.2 ± 0.2^b	-1.228 (0.034)	-1.216 (0.033)	-1.198 (0.026)	-1.4 ± 0.2^b	-1.433 (0.187)	-1.459 (0.197)	-1.490 (0.188)
L_1	2.06^i , 2.1^g 2.4 ± 0.15^g	2.247	2.095	2.234	0.744^d	0.776	0.64	0.747
L_3	3.9^i , 4.15 ± 0.1^g	4.324 (0.016)	3.962 (0.015)	4.245 (0.007)	4.2 ± 0.1^g , 4.4^c 4.3 ± 0.2^d	4.319 (0.087)	4.227 (0.103)	4.250 (0.077)
L'_2		7.334	8.161	8.031	7.8^c , 7.8 ± 0.1^g 7.9^i	7.285	7.495	7.242
X_1		-7.711	-7.823	-8.087	-9.3 ± 0.2^g	-8.646	-8.995	-8.875
X_4	-2.5 ± 0.3^b , -2.9^g -3.3 ± 0.2^g	-2.889	-2.92	-2.95	-3.66^c , -3.15 ± 0.2^d -3.5 ± 0.2^g	-3.267	-3.28	-3.375
X_1	1.13^i , 1.25^c , 1.3^g	1.163	1.221	1.321	1.3 ± 0.2^d	1.254	1.045	1.169
W_1	-8.1 ± 0.3^b	-7.512 (0.006)	-7.653 (0.005)	-7.662 (0.295)	-8.7 ± 0.3^b	-8.512 (0.029)	-8.88 (0.025)	-8.638 (0.103)
W_2	-3.9 ± 0.2^b	-3.886 (0.014)	-3.95 (0.013)	-3.922 (0.008)	-3.9 ± 0.2^b	-3.956 (0.042)	-4.151 (0.075)	-4.038 (0.154)
Σ_1^{min}	-4.7 ± 0.2^b	-4.466	-4.527	-4.553	-4.5 ± 0.2^b	-4.548	-4.748	-4.555
$\overline{E_g}(\Delta)$	1.17^d	1.031	1.076	1.17		1.04	0.855	0.961
$\overline{E_1}(L)$	3.45^g , 3.46^c	3.492	3.311	3.432	2.05^d , 2.22^f	2.302	2.099	2.239
$\overline{E'_1}(L)$	5.38^c , 5.50^g	5.577	5.178	5.443	5.65^d	5.889	5.686	5.750
$E_2(X)$	4.32^c	4.052	4.141	4.271	4.45^f	4.521	4.325	4.544

^aSymbols of Ref. 49.

^bAs presented in Ref. 10.

^cAs presented in Ref. 39.

^dAs presented in Ref. 28.

^eReference 40.

^fReference 41.

^gAs presented in Ref. 42.

metry operations, the Hamiltonian of an isolated centrosymmetric crystal exhibits time-reversal symmetry. The additional degeneracy among eigenvalues may be determined using the Kramer theorem and the Wigner rule. Using that rule, Ma *et al.*¹⁵ have obtained additional information about the degeneracy in Si and Ge for the [001], [111], and [110] growth cases that have been accounted for in the present $k \cdot p$ model.

Typical results of our fit procedure are presented in Fig. 4(a) [and Fig. 4(b)] for the biaxially strained Si [Ge] layer grown on a [001]-oriented cubic Ge buffer [and Si buffer, respectively]. Further results are shown in Fig. 5(a) [and Fig. 5(b)] for the strained Si [Ge] layer on a [111]-oriented cubic Ge buffer [and Si buffer]. The band structures calculated along various directions in reciprocal space using the present $k \cdot p$ model are compared to EPM (Ref. 50) and GW results. For a purely biaxially strained Si layer (Fig. 4), the minima of the L valleys remain equivalent. However, due to crystal symmetry lowering, the equienergy lowest CB Δ valleys are split into four Δ_4 and two Δ_2 valleys. On the contrary, strain

along the [111] direction leaves the Δ valleys equivalent whereas valleys at second minima are split (two Z valleys along [111] and six L valleys along $[\bar{1}11]$, $[1\bar{1}1]$, and $[11\bar{1}]$). Moreover, it can be seen that the two lowest CBs along the Γ - X direction become nondegenerate at X , the splitting being the result of the removal of the center of inversion in the sheared crystal.¹⁵ Another important effect of the strain is observable in the near- Γ region, for instance in Fig. 4: In the case of the strained Si (tensile-biaxial strain), the heavy-hole band “crosses” the SO band, while in the case of strained Ge it is the contrary (compressive-biaxial strain): the SO-hole band “crosses” the heavy-hole one.

IV. RESULTS AND COMPARISON TO EXPERIMENTAL DATA

A. Energy band gaps

We now address the question as to how well the energy levels (*vide post* for the effective masses) calculated using

TABLE IV. Effective curvature masses and Luttinger parameters.

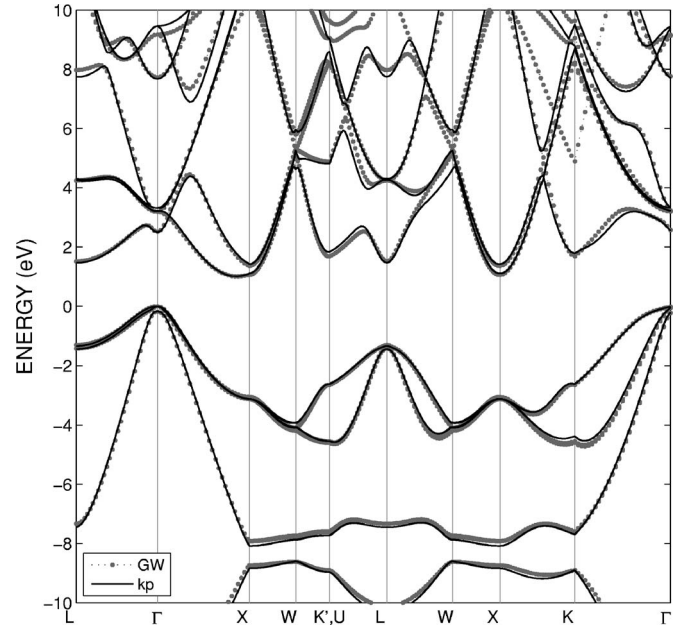
Si	Expt.	G_0W_0	EPM	$k \cdot p^d$
m_T^Δ	0.9163 ^a	0.925	0.89	0.928
m_T^Δ	0.1905 ^a	0.189	0.198	0.192
m_T^L		1.8083	1.855	1.704
m_T^L		0.1235	0.1535	0.131
γ_1	4.26, ^a 4.285 ^a 4.22, ^b 4.340 ^c	4.54	4.01	4.338
γ_2	0.38, ^a 0.339 ^a 0.39, ^b 0.31 ^c	0.33	0.38	0.3468
γ_3	1.56, ^a 1.446 ^a 1.44, ^b 1.46 ^c	1.54	1.401	1.4451
Ge	Expt.	G_0W_0	EPM	$k \cdot p^d$
m_T^Δ		0.881	0.964	0.874
m_T^Δ		0.176	0.205	0.200
m_T^L	1.588, ^f 1.74 ^g	1.626	1.763	1.59
m_T^L	0.08152, ^f 0.079 ^g	0.074	0.099	0.099
γ_1	13.0, ^h 12.8, ^e 13.25 ^a	13.54	9.54	10.41
γ_2	4.4, ^h 4.0, ^e 4.20 ^a	4.32	2.75	3.045
γ_3	5.3, ^h 5.5, ^e 5.56 ^a	5.77	3.93	4.313

^aAs presented in Ref. 28.^bBalslev and Lawaetz, as presented in Ref. 22.^cReference 52.^dPresent model.^eReference 53.^fReference 54.^gReference 55.^hReference 17.

$k \cdot p$ agree with the experiments and theoretical results. Tables I and III show a comparison for the cases where experimental data seem to be well established. To this end, we

TABLE V. Elastic coefficients and internal strain parameter.

	Si		Ge	
	Expt.	LDA ^a	Expt.	LDA ^a
D_{001} (GPa)	0.776	0.795	0.7513	0.711
D_{110} (GPa)	0.515	0.527	0.4498	0.42
D_{111} (GPa)	0.444	0.461	0.3711	0.343
C_{11} (GPa)	167.5 ^d	168.3 ^b	131.5 ^d	132.8 ^b
C_{12} (GPa)	65 ^d	66.8 ^b	49.4 ^d	46.8 ^b
C_{44} (GPa)	80.1 ^d	79.9 ^b	68.4 ^d	66.57 ^b
ξ	0.54 ^c	0.536	0.54 ^c	0.495

^aPresent work.^bElastic constant calculated from the D values.^cReference 70.^dReference 71.FIG. 3. Bulk Si_{0.5}Ge_{0.5} electronic band structure obtained using the 30-level $k \cdot p$ model and GW calculation.

have used the large set of experimental values summarized by Chelikowsky and Cohen,¹⁰ Landolt-Börnstein,²⁸ Hybertsen and Louie,⁴² and Aulbur *et al.*,²⁹ but also the most recent optical measurements in Si (Ref. 40) and Ge (Ref. 41). We note that this assignment is in several cases somewhat tentative. The interpretation of the experimental peaks and critical points is hindered when energetically close transitions take place, e.g., due to SO-split bands. Moreover, the critical points might originate from transitions close to, but not necessarily exactly at, high-symmetry points in the Brillouin zone. Aside from recent inverse-photoemission and photoemission experiments which have addressed certain high-energy bands in Si and Ge,³⁹ the complex shape of the different energy bands cannot be easily measured directly on its whole structure.

It is clear from Tables I and III that the overall agreement between theoretical and experimental band gaps is good. In particular, the present $k \cdot p$ model predicts indirect gaps of 1.17 eV in Si and 0.747 eV in Ge.

B. Curvature masses, Luttinger parameters, and DOS

The Δ -electron and L -electron effective masses were obtained from the second derivative of the CB energy with respect to the wave vector along various directions away from the valley minima. The VBs are extremely nonparabolic, and so the effective masses could not be evaluated by the method described above. Instead, we used the six-level $k \cdot p$ Dresselhaus-Kip-Kittel model,¹⁷ which depends on three Luttinger parameters, the values of which have been fitted using a conjugate-gradient optimization. This optimization is based on a least-squares error between the curvature masses along the [001], [111], and [110] directions obtained with this six-level $k \cdot p$ model and with the EPM, 30-level $k \cdot p$, or GW models. We verified in the EPM and $k \cdot p$ method

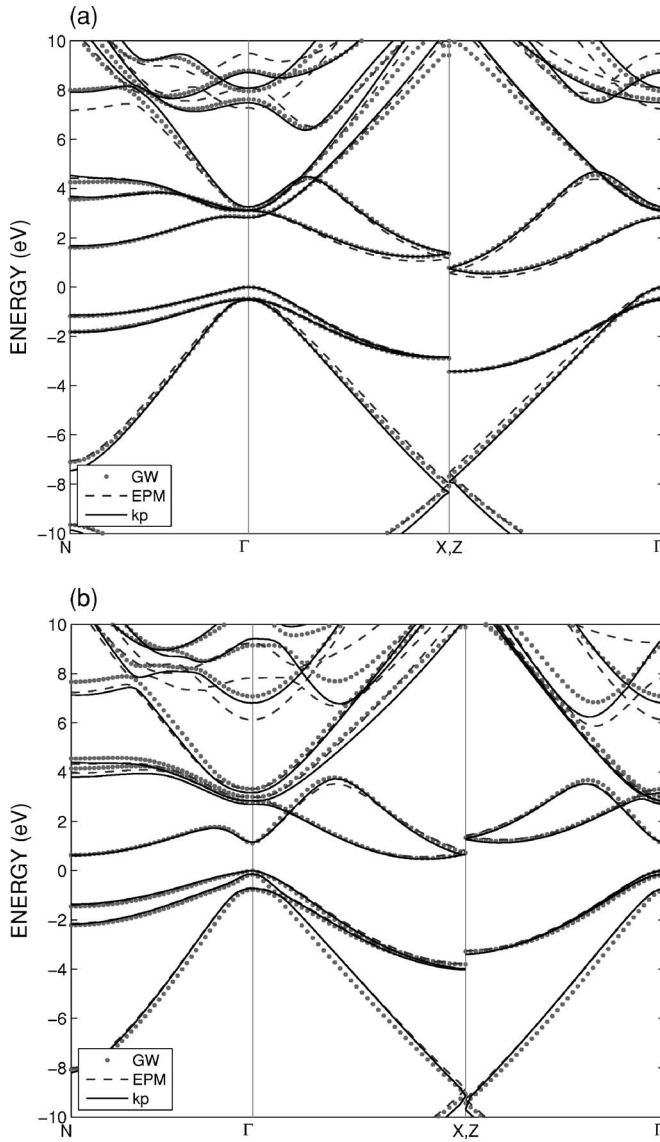


FIG. 4. (a) Band structure of a strained Si layer grown on a [001]-oriented cubic Ge buffer and (b) band structure of a strained Ge layer grown on a [001]-oriented cubic Si buffer. The Si layer is biaxially strained in tension, while the Ge layer is biaxially strained in compression. Simulations have been performed with the 30-level $k \cdot p$ model (solid lines), EPM (dashed lines), and GW (dotted lines) along various directions connecting high-symmetry points of the distorted Brillouin zone (Ref. 15).

that the present extraction technique of the curvature masses and Luttinger parameters gives similar results to a direct calculation based on the sum rules and the $k \cdot p$ theory^{14,17,51} (e.g., the Chelikowsky-Cohen EPM values obtained by Rieger and Vogl¹⁴ in Ge, $\gamma_1=9.563$, $\gamma_2=2.77$, and $\gamma_3=3.91$, can be compared to our results listed in Table IV). The theoretical effective masses and Luttinger parameters are listed in Table IV, and we can see that all methods provide reasonably good agreement with experimental values. It should be mentioned nevertheless that the present $k \cdot p$ model as well as the present nonlocal EPM gives rather disappointing results for the VB Luttinger parameters in Ge. Even if the present $k \cdot p$ parameter set improves the accuracy of the Luttinger

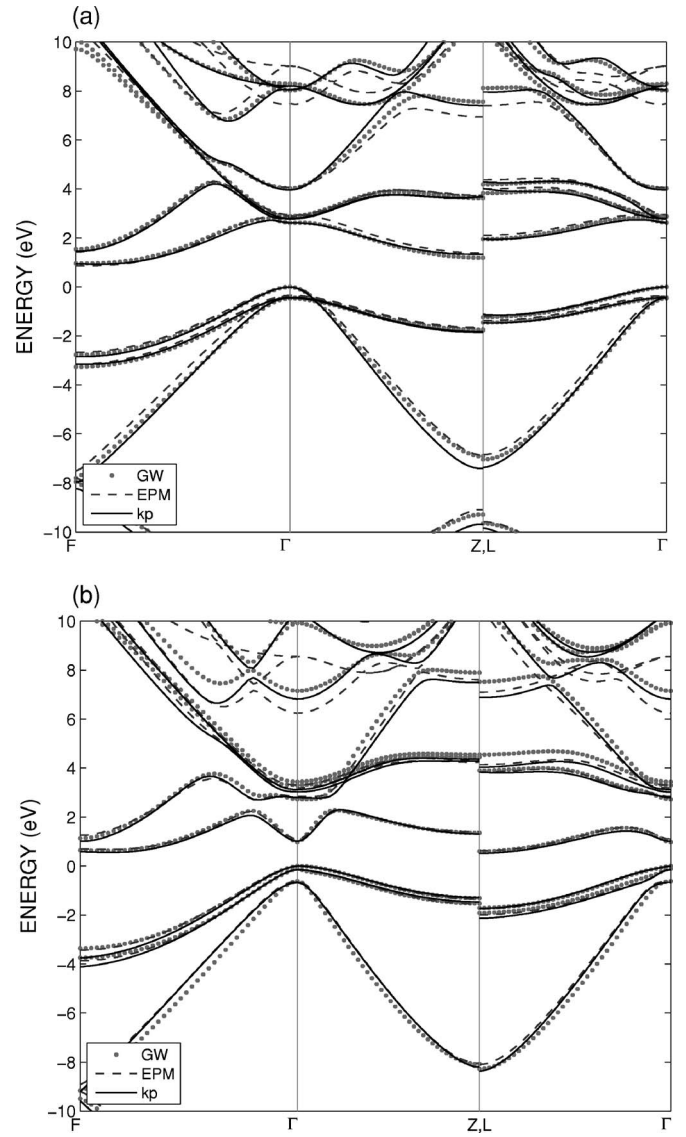


FIG. 5. Same as Fig. 4 but in case of (a) a strained Si layer grown on a [111]-oriented cubic Ge buffer and (b) a strained Ge layer grown on a [111]-oriented cubic Si buffer.

parameters, it still underestimates their values by about 20%. When the Luttinger parameters are expressed in terms of matrix elements,^{14,17,51} it becomes clear why it is so: They contain the term $P/E_{\Gamma_2'}$, the value of which is relatively small in the present work.⁴⁷

An accurate description of the DOS is key features for accurate carrier density modeling within a realistic transport model in semiconductors.^{56,57} The DOS is also a good check for the quality of the present $k \cdot p$ parameter set. Indeed, the DOS not only depends on the band energies but also on their gradient with respect to the wave vector (group velocity).

The DOS is obtained using the Gilat-Raubenheimer procedure.⁵⁸ We applied exactly the same algorithm using the $k \cdot p$ (solid lines), the EPM (dashed lines), and the GW models (dotted lines), respectively. As can be seen in Fig. 6, the agreement between the three models is excellent for the VBs but also for the CBs from -5 eV up to 5 eV.

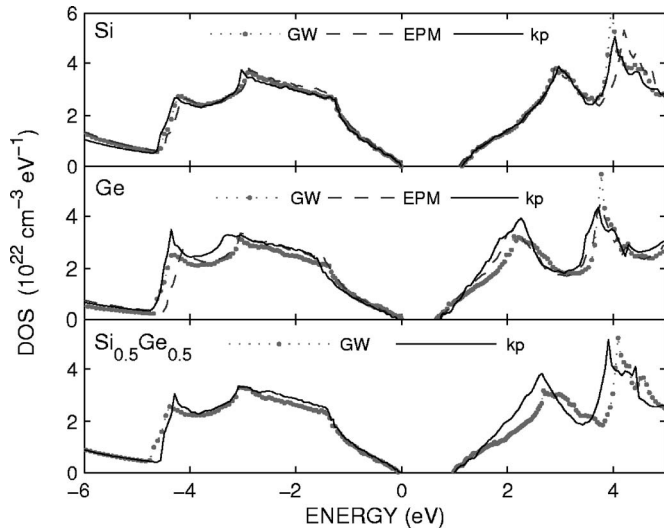


FIG. 6. The DOS of Si, Ge, and Si_{0.5}Ge_{0.5} alloy: Comparison between 30-level $k \cdot p$ (solid lines), EPM (dashed lines), and GW (dotted lines).

C. Energy band shifts in strained Si_{1-x}Ge_x/Si_{1-y}Ge_y systems

The calculated energy shifts of the main VBs and CBs extrema in Si, Ge, and Si_{1-y}Ge_y are shown in Figs. 7–9 for material grown on [001], [111], and [110] Si_{1-y}Ge_y buffers, respectively. In these figures, good agreement can be noticed between first-principles simulations, EPM, and the present $k \cdot p$ models. An important effect of strain can be clearly seen, for example, in Fig. 7: Several Γ eigenvalue shifts exhibit a highly nonlinear (and even nonmonotonic) relation versus y . This implies that the dependence of the energy gaps on strain is substantially nonlinear, which has been reported for Ge and GaAs.⁵⁹ This typical result⁵¹ is induced by the coupling between states due to symmetry lowering. Indeed, several k -independent coupling terms (W_{Γ} terms in the $W_{30 \times 30}$ perturbation matrix) occur in strained materials (e.g., for

sheared crystals between the Γ_{15} and $\Gamma_{2'1}$ states originally uncoupled in the relaxed $k \cdot p$ Hamiltonian).

From the energy band shifts, we have calculated the deformation potentials which reflect the variation of an individual band energy as a function of applied strain. Following the notation of Van de Walle,⁷ the experimental values found in strained Si and Ge for the splitting of the top of the VBs are quoted in Table II. The deformation potentials a_v , b_v , and d_v refer to the hydrostatic, the splitting, and the shear deformation potentials of the VBs at Γ , respectively. Theoretical deformation potentials are consistent with the experimental ones except for d_v in Ge, which is overestimated by $\approx 8\%$. This result can be inferred from the slight overestimation of the theoretical internal parameter ξ shown in Table VI (see Appendix A). Besides deformation potentials at Γ , other deformation potentials have been experimentally determined at the lowest CB minima, typically along the L direction for Ge and X direction for Si. In Table II, Ξ_d^{Δ} and Ξ_d^L are the hydrostatic CB deformation potentials, while Ξ_u^L and Ξ_u^{Δ} are the splitting deformation potential.

It is worth mentioning that certain quantities listed in Table II depend on the absolute VB hydrostatic deformation potentials a_v . Individual quantities are difficult to measure because they are referred to an absolute energy scale that is in most cases determined using empirical rules (e.g., the deep defect level pinning).^{60,61} Theoretically, the relation to an absolute energy is well defined only when specific boundary conditions are introduced, which relate the potential to a common zero of energy. Most modern band structure methods usually apply the periodic boundary condition, so the electronic states are defined within an unknown constant.⁶² In this work, we did not calculate a_v ; the energy scales have been fixed by setting arbitrarily to zero the top of the VBs and using the hydrostatic deformation potential values determined from carrier mobility by Fischetti and Laux¹³ ($a_v=2$ for Si, $a_v=2.1$ for Ge). These values, which are consistent with recent first-principles calculations,⁶² were later interpolated for Si_{1-x}Ge_x alloys ($a_v=2+0.1x$).

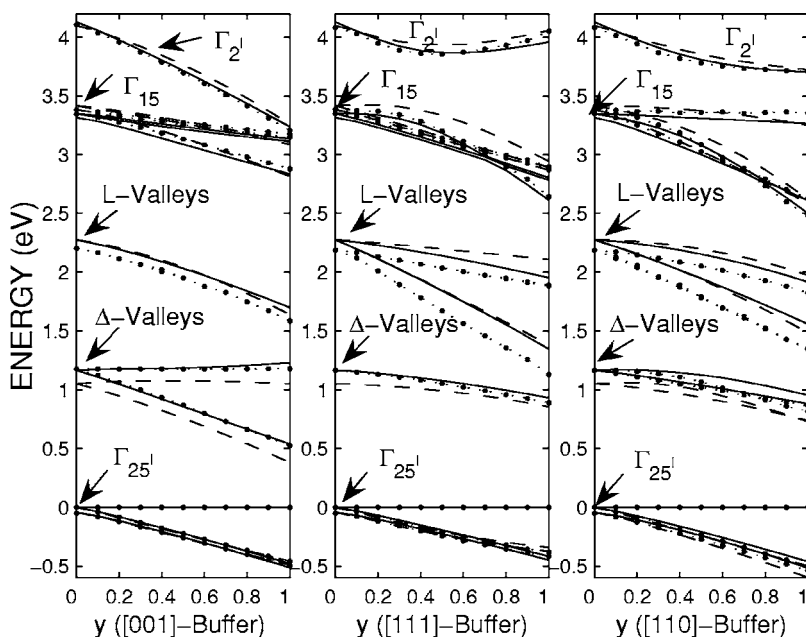


FIG. 7. Calculated VB and CB shifts of a strained Si layer as a function of y content in the Si_{1-y}Ge_y buffer: $k \cdot p$ (solid lines), EPM (dashed lines), and GW (dotted lines) simulations performed for various buffer orientations.

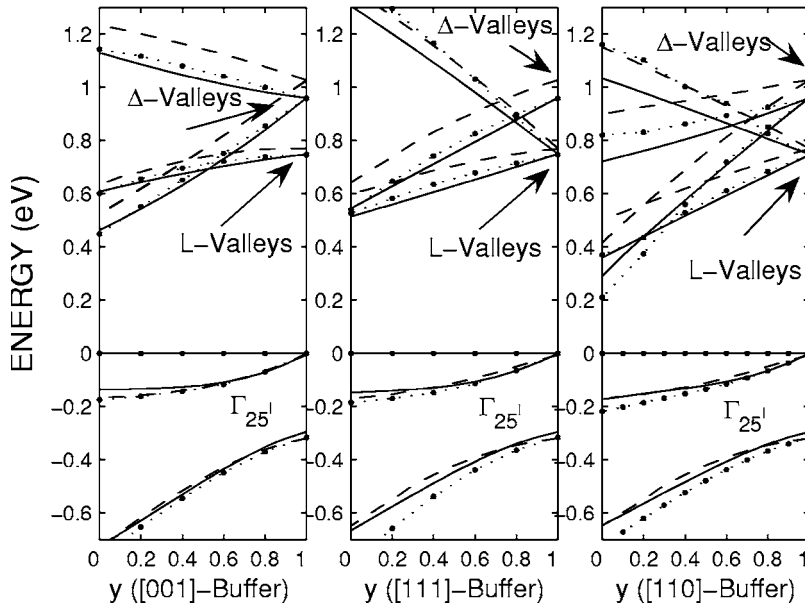


FIG. 8. Calculated VB and CB shifts of a strained Ge layer as a function of y content in the $\text{Si}_{1-y}\text{Ge}_y$ buffer: $k\cdot p$ (solid lines), EPM (dashed lines), and GW (dotted lines) simulations performed for various buffer orientations.

D. Carrier masses in strained $\text{Si}_{1-x}\text{Ge}_x/\text{Si}_{1-y}\text{Ge}_y$ systems

The electronic transport properties in strained devices depend not only on the gap variation with strain, but also on the carriers effective masses,¹³ which reflect the local curvature of the band structure near a minimum in energy. Figures 10 and 11 show the strained Si and Ge electron curvature masses change as a function of y content in the $\text{Si}_{1-y}\text{Ge}_y$ buffer for various orientations. Focusing, for example, on the Δ valleys in purely biaxially strained Si layer ([001] buffer in Fig. 10), it can be seen that the change in curvature masses depend on the Δ valleys in question but remain relatively small ($<10\%$), which is in good agreement with cyclotron resonance data for Si on [001]- $\text{Si}_{0.7}\text{Ge}_{0.3}$.⁶³ On the contrary, for the [111]-growth case ([111] buffer in Fig. 10), each Δ valley exhibits the same longitudinal and transverse masses but their values are significantly larger (up to 100%) than in

the bulk Si. Finally, the [110]-growth case is a mixture of the two previous cases.⁷ The Δ valleys exhibit different longitudinal and transverse curvature masses that can increase even more than for the [111]-growth case. It can be noted that the large increase of the curvature masses with shear strain is much more pronounced for the Δ valleys than for the L valleys. We found out that, in addition to the increase of the Δ -electron masses with applied strain, the Δ -valley minima positions in reciprocal space also significantly change. This behavior is generally more pronounced when shear distortions are applied. For instance, the Δ -valley minimum distance along the Γ - X direction changes from 84% in bulk Si up to 97% in strained Si on [111]-oriented Ge buffer. This latter point and the changes in shape can be seen in the three-dimensional (3D) surface plot at thermal energy ($\frac{3}{2}kT$) shown in Fig. 12. The Δ valleys in the first and second Brillouin zones are shown, respectively, along the Γ - X , Γ - Y , and

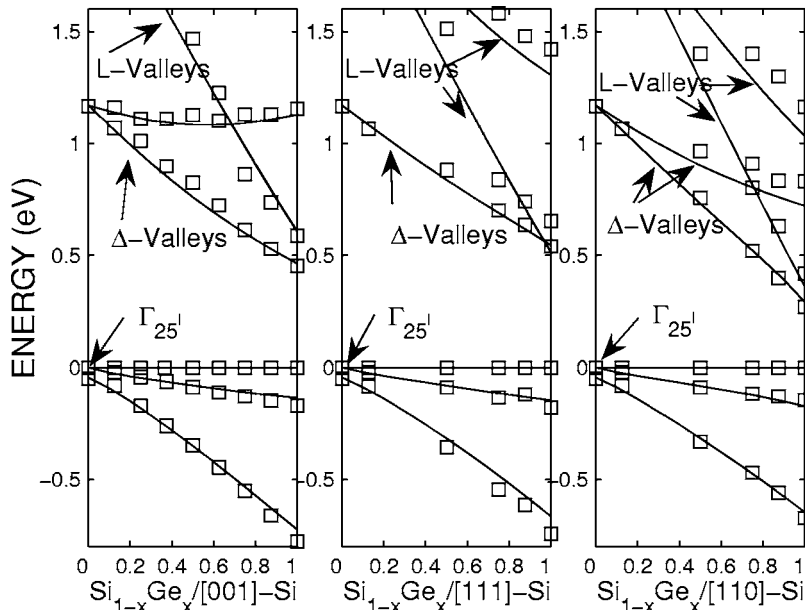


FIG. 9. Calculated VB and CB shifts of a strained $\text{Si}_{1-x}\text{Ge}_x$ layer grown on a Si buffer: $k\cdot p$ (solid lines) and GW (symbols) simulations performed for various buffer orientations.

TABLE VI. Matrix elements of the linear momentum \mathbf{p} (a.u.) used in the present $\mathbf{k}\cdot\mathbf{p}$ model. Symbols of group O^h are taken from Ref. 19. Other symbols for Si_{1-x}Ge_x ($0 < x < 1$) belong to group T^d .

Matrix elements (a.u.)	Si _{1-x} Ge _x
$P \equiv \frac{\hbar}{m} \langle \Gamma_{25't'} \mathbf{p} \Gamma_{2't'} \rangle$	$1.22 - 0.034x$
$Q \equiv \frac{\hbar}{m} \langle \Gamma_{25't'} \mathbf{p} \Gamma_{15} \rangle$	$1.0679 + 0.0068x$
$R \equiv \frac{\hbar}{m} \langle \Gamma_{25't'} \mathbf{p} \Gamma_{12't'} \rangle$	$0.5427 + 0.0884x$
$P'' \equiv \frac{\hbar}{m} \langle \Gamma_{25't'} \mathbf{p} \Gamma_{2't''} \rangle$	$0.156 - 0.0081x$
$P' \equiv \frac{\hbar}{m} \langle \Gamma_{25't''} \mathbf{p} \Gamma_{2't'} \rangle$	$-0.008 + 0.078x - 0.05x^2$
$Q' \equiv \frac{\hbar}{m} \langle \Gamma_{25't''} \mathbf{p} \Gamma_{15} \rangle$	$-0.6555 - 0.1052x$
$R' \equiv \frac{\hbar}{m} \langle \Gamma_{25't''} \mathbf{p} \Gamma_{12't'} \rangle$	$0.8342 - 0.0126x$
$P''' \equiv \frac{\hbar}{m} \langle \Gamma_{25't''} \mathbf{p} \Gamma_{2't''} \rangle$	$1.425 - 0.0263x$
$T \equiv \frac{\hbar}{m} \langle \Gamma_{1'u} \mathbf{p} \Gamma_{15} \rangle$	$1.166 - 0.0247x - 0.04x^2$
$T' \equiv \frac{\hbar}{m} \langle \Gamma_{1't'} \mathbf{p} \Gamma_{15} \rangle$	$0.29 + 0.08x$
$S \equiv \frac{\hbar}{m} \langle \Gamma_{15} \mathbf{p} \Gamma_{2't'} \rangle$	$-i0.1x(1-x)$
$S' \equiv \frac{\hbar}{m} \langle \Gamma_{15} \mathbf{p} \Gamma_{2't''} \rangle$	$i0.3x(1-x)$
SO coupling strength (eV)	Si _{1-x} Ge _x
$\Delta_{\Gamma_{25't'}, \Gamma_{25't''}}$	$0.022 + 0.198x$
$\Delta_{\Gamma_{15}, \Gamma_{25't'}}$	$0.04x - 0.04x^2$

Γ -Z directions for bulk Si and for the [001]- and [111]-growth cases. The Δ -valley 3D surfaces in the first and second Brillouin zones are clearly separated in the bulk and in the purely [001] biaxially strained crystal, while they “merge” into a single 3D surface for the [111]-strained crystal.

For the reason mentioned previously, the curvature masses for the three topmost VBs cannot be easily evaluated from parabolic fits. Instead, the variations of the DOS effective masses in coherently strained Si and Ge layers are shown in Figs. 13 and 14 as a function of the mole fraction y in the relaxed Si_{1-y}Ge_y buffer. In the unstrained crystal, the heavy-hole DOS mass is approximately 3 times larger than the light-hole mass. This difference decreases as soon as the degeneracy at Γ between the heavy and light holes is removed and the bands mixing becomes significant. As already studied with the sum rule,^{11,51} strain-induced changes in the Luttinger parameters, as observed in cyclotron resonance experiments,⁶⁴ are also involved in the results shown in Figs. 13 and 14.

At least four independent theoretical EPM calculations in purely biaxially strained Si and Ge crystals have reported changes in effective masses.^{11,13,14,51} However, few results have been published for shear distortions.⁵¹ The present calculations show similar behavior for biaxial strain and extend the results to shear distortions. Although few direct measurements of the curvature masses are available^{63,64} in strained Si and Ge, recent transport simulations in inversion layers using “full-band” Monte Carlo simulations⁶⁵ have suggested that changes in effective masses due to strain should be involved to account for the mobility variations measured in strained devices. Concerning the effective masses at the second CB minima in energy (i.e., L valley in Si and Δ valley in Ge), similar good agreements between empirical methods (EPM and $\mathbf{k}\cdot\mathbf{p}$) and GW results have been found. It should be

noted that these valleys could play a significant role in the transport properties of strained semiconductors, particularly for Ge, in which the Δ valley and L valley are separated by only 200 meV. Indeed, in the case of a biaxially strained Ge layer grown on a [001]-oriented Si_{1-y}Ge_y buffer the Δ -valley minima lie at a lower energy than the L -valleys minima for $y \leq 0.5$ (see Fig. 8), which implies that these valleys would contribute substantially to the current.

V. DISCUSSION

We have presented a 30-level $\mathbf{k}\cdot\mathbf{p}$ model for bulk and strained SiGe, the parameters of which have been optimized using a conjugate-gradient procedure on a reference set of energy bands obtained with first-principles calculations. The first-principles simulations have been validated through an accurate comparison with experimental results found in the literature. For bulk Si, Ge, and SiGe alloys, a set of comparisons with experimental data has shown good agreement for the main band gaps values (Tables I and III), the carrier effective masses, and Luttinger parameters (Table IV). For strained materials, we have benchmarked our first-principles results using the deformation potential theory applied to the specific case of Si and Ge epitaxial layers grown on [001]-, [111]-, and [110]-oriented relaxed buffers. Theoretical deformation potentials (Table II) have been found to be consistent with experimental ones, within experimental error. A second set of comparisons has been performed using the widely used Chelikowsky-Cohen nonlocal EPM,¹⁰ including relativistic corrections.

As presented in this paper, the present 30-level $\mathbf{k}\cdot\mathbf{p}$ model can be used to fit first-principles simulations accurately. This is also an illustration that the $\mathbf{k}\cdot\mathbf{p}$ method might be a good and efficient method for another systems of material as well.

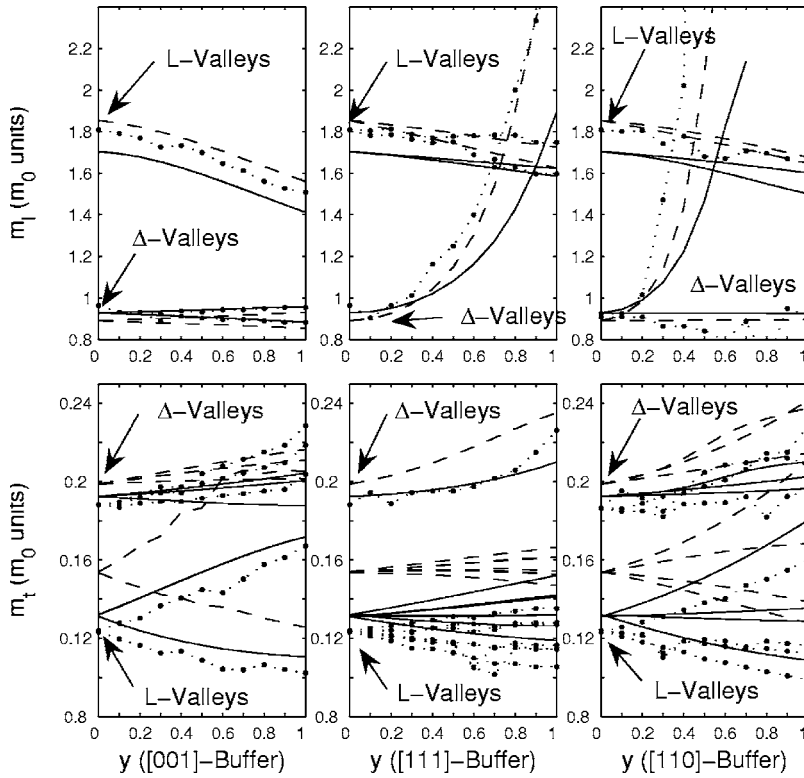


FIG. 10. Strained Si electron longitudinal and transverse curvature masses as a function of y content in the $\text{Si}_{1-y}\text{Ge}_y$ buffer: $k\cdot p$ (solid lines), EPM (dashed lines), and GW (dotted lines) simulations performed for various buffer orientations.

Moreover, our procedure yields additional pieces of information.

(i) Using first-principles simulations, important quantities not addressed experimentally yet (high-energy levels and effective masses at the second CB minima) have been taken into account in the present $k\cdot p$ model.

(ii) SiGe compounds have been modeled using interpolation functions between Si and Ge $k\cdot p$ parameters. Additional SO splittings and energy degeneracy removal (due to centrosymmetry breaking) have been accounted for with supplementary coupling $k\cdot p$ parameters fitted on first-principles data.

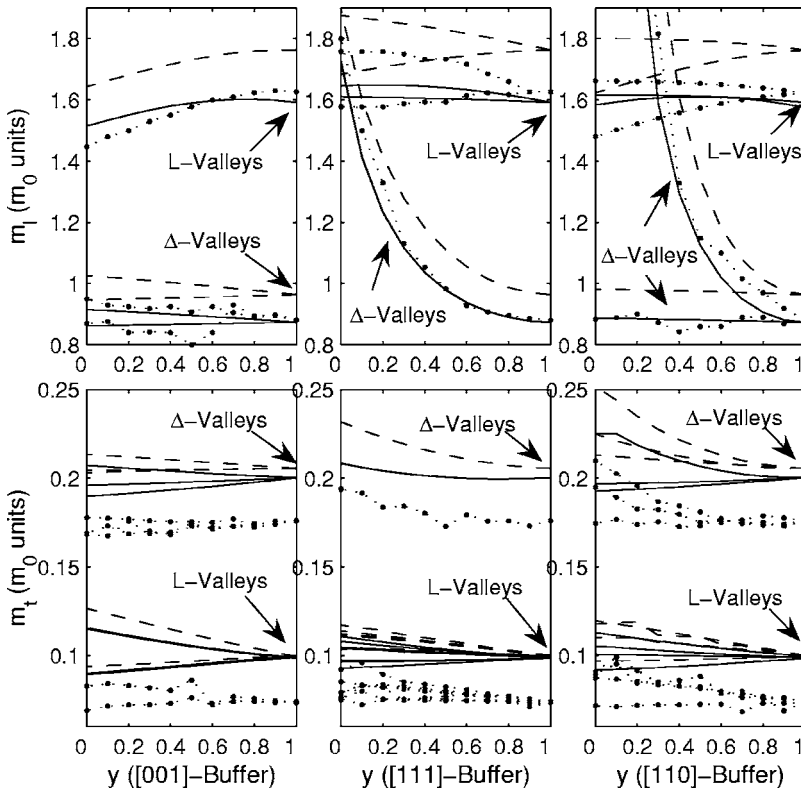


FIG. 11. Strained Ge electron longitudinal and transverse curvature masses as a function of y content in the $\text{Si}_{1-y}\text{Ge}_y$ buffer: $k\cdot p$ (solid lines), EPM (dashed lines), and GW (dotted lines) simulations performed for various buffer orientations.

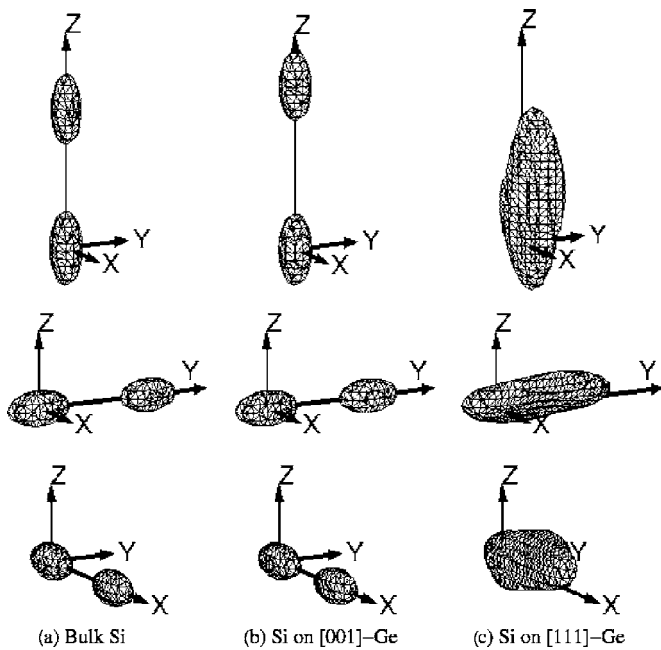


FIG. 12. 3D-surface plot at thermal energy of the lowest CBs across the Brillouin zone edges along the [100], [010], and [001] directions. Simulations performed for (a) bulk Si, (b) strained Si on [001]-oriented cubic Ge buffer, and (c) strained Si on [111]-oriented Ge buffer.

(iii) As emphasized by Fischetti and Laux,¹³ a rigorous description of the carrier mobility in strained Si and Ge devices is closely related to the accuracy of the BS calculation. The “full-band” Monte Carlo (MC) approach, which solves the Boltzmann transport equation, is one of the most promising ways to estimate the current in nanoscale devices. Most of the “state-of-the-art” MC simulators^{13,54,57} are based on the EPM BS calculation. In this paper, we have shown that the nonlocal EPM and $k \cdot p$ results were actually very close. Recent full-band MC simulations based on the present $k \cdot p$ model have shown good agreement with EPM-based MC simulations. It should be noted that from a practical point of view, the computational burden of the $k \cdot p$ calculations is impressively reduced in comparison to EPM simulations: The CPU time to obtain a complete band structure is approximately two orders of magnitude less than the CPU time needed by EPM.⁶⁶

For the reasons mentioned above, the present highly optimized $k \cdot p$ parameter set improves the published $k \cdot p$ parameters set of Refs. 19 and 21 for bulk materials and extends its predictions to SiGe alloys. Furthermore, the Pikus-Bir perturbative treatment of strain was for the first time evaluated in the Cardona-Pollak 30-level $k \cdot p$ formalism.¹⁹ We have shown notably that this correction captures the main feature of strained-crystal band structures, such as energy shifts⁷ and effective masses change^{11,13,14,51} due to

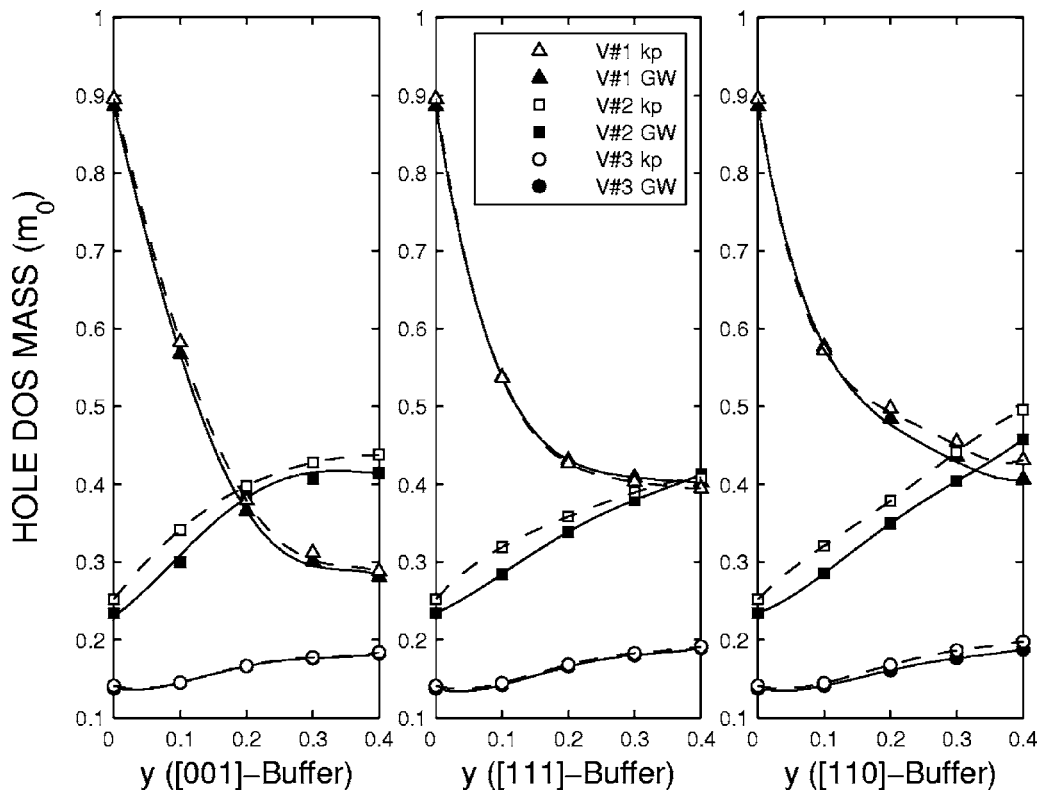


FIG. 13. Coherently strained Si layer hole masses as a function of Ge content y in the [001], [111], and [110] $\text{Si}_{1-y}\text{Ge}_y$ buffers: $k \cdot p$ (open symbols) and GW (solid symbols). Solid lines and dashed lines are a guide for the eyes; $T=300$ K.

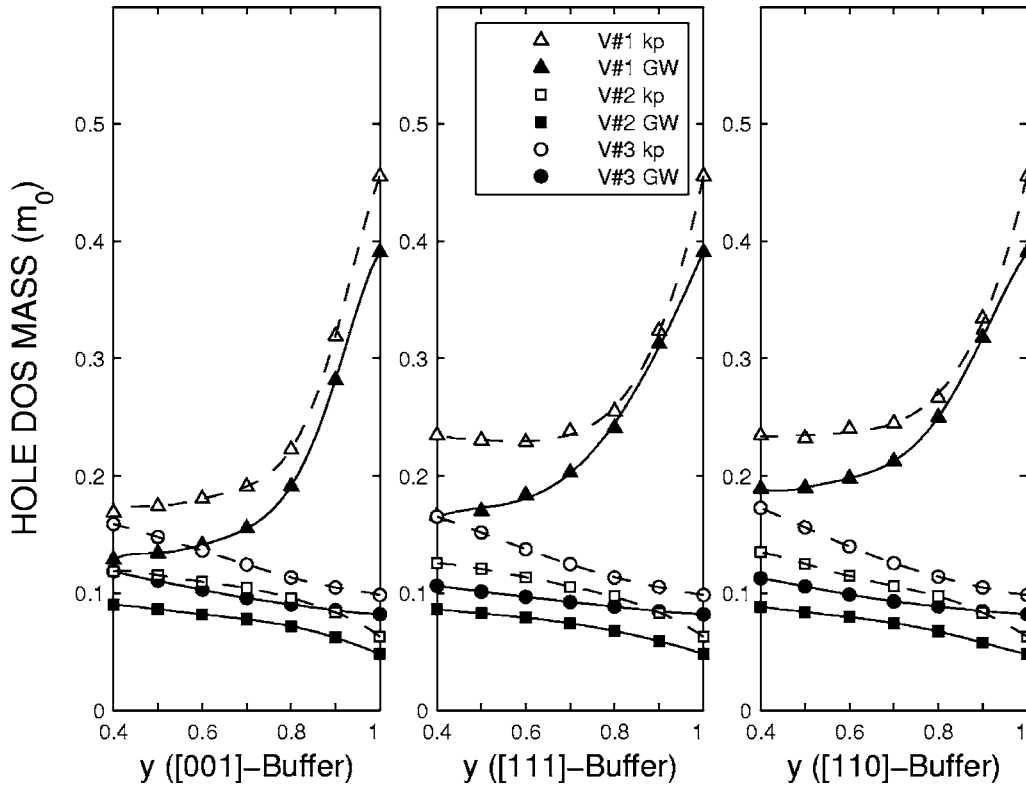


FIG. 14. Coherently strained Ge layer hole masses as a function of Ge content y in the [001], [111], and [110] $\text{Si}_{1-y}\text{Ge}_y$ buffers: $k \cdot p$ (open symbols) and GW (solid symbols). Solid lines and dashed lines are a guide for the eyes; $T=300$ K.

strain. It ought to be mentioned that this is not the case with the recently published 20-level $k \cdot p$ model for biaxially strained Si and Ge,⁶⁷ in which important contributions to the strain perturbation matrix have been omitted. We found out that the behavior of the CBs in strained Si and Ge strongly depends on the W_k and $W_{\Gamma,\Gamma}$ terms in the perturbation matrix. The neglect of such matrix elements leads to a large underestimation of the CB equienergy valley splitting and effective masses changes versus strain. Moreover, the time reversal symmetry (e.g., as can be seen in Fig. 4 degeneracies at the point X remain in the [001]-growth case) and correct band shifts at L valleys versus strain cannot be obtained without these contributions.

VI. CONCLUSION

In this paper, we have developed a highly optimized 30-level $k \cdot p$ model for strained Si, Ge, and SiGe alloys.

A series of *ab initio* DFT-LDA simulations that include GW correction and relativistic effects in Si, Ge, and SiGe alloys has been performed with a view to obtaining information not addressed by experiments. Once a reference set of energy bands has been obtained, we have optimized the $k \cdot p$ model parameters using a conjugate-gradient procedure in order to fit as closely as possible first-principles results, but also carrier effective masses and Luttinger parameters. A

simple interpolation between Si and Ge $k \cdot p$ parameters has been proposed in order to model SiGe alloys.

The electronic structure of strained $\text{Si}_{1-x}\text{Ge}_x$ layers grown on $\text{Si}_{1-y}\text{Ge}_y$ buffers has been studied using first-principles simulations. The Pikus-Bir correction²³ for strained materials has been examined within this 30-level $k \cdot p$ formalism, and the deformation potentials have been obtained from first-principles simulations in order to fit the shifts of the 30 lowest-energy levels at Γ versus applied strain, but also the general shape of the band structure of the strained crystal.

Finally, the present $k \cdot p$ model has been validated through an accurate set of comparisons with experimental data in relaxed and strained Si, Ge, and $\text{Si}_{1-x}\text{Ge}_x$ alloys. A second set of comparisons with first-principles simulations, but also with the widely used Chelikowsky-Cohen nonlocal EPM,¹⁰ has also shown a good agreement. The present $k \cdot p$ description of strained Si, Ge, and SiGe accurately reproduces the overall band structure, as well as the band shifts and the carrier effective masses versus applied strain.

ACKNOWLEDGMENTS

We would like to thank Y. M. Niquet for a number of useful discussions and P. Roulliaux, D. P. Nguyen, and N. Kauffman for a critical reading of the manuscript.

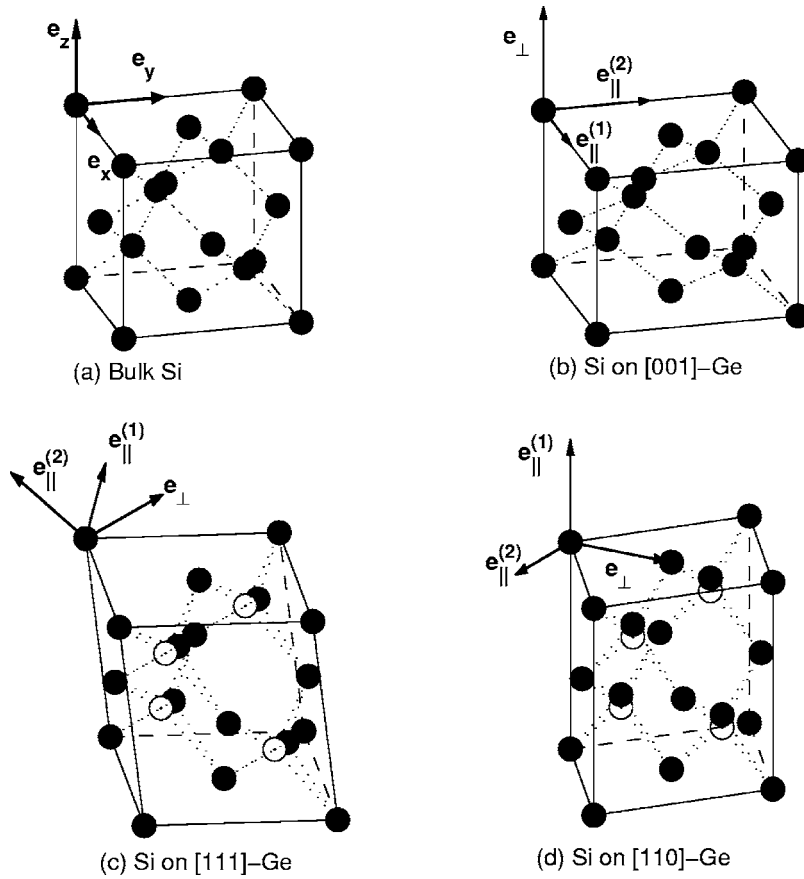


FIG. 15. Distorted diamond structures coherently grown on oriented substrates: (a) unstrained cubic structure, (b) Si grown on [001]-Ge substrate, (c) Si grown on [111]-Ge substrate, and (d) Si grown on [110]-Ge substrate. For the [111]- and [110]-growth cases, the inner displacements of atoms in the distorted cell are shown for $\xi=0$ (white atoms) and $\xi=1$ (black atoms). Also shown are the basis vectors in which the strain tensor is biaxial (see text for detail). For clarity, the distortion magnitude has been arbitrarily amplified.

APPENDIX A: $k \cdot p$ STRAIN TENSOR AND STRUCTURAL OPTIMIZATION OF THE UNIT CELL IN EPITAXIAL LAYERS

When Si and Ge are grown epitaxially on the cubic Si_{1-y}Ge_y substrate, the layer atoms are described as being subjected to biaxial tension and compression, respectively. Using continuum elasticity theory, the biaxial strain tensor can be written as

$$\epsilon^{DCS} = \begin{pmatrix} \epsilon_{\parallel} & 0 & 0 \\ 0 & \epsilon_{\parallel} & 0 \\ 0 & 0 & \epsilon_{\perp} \end{pmatrix}, \quad (\text{A1})$$

where the longitudinal strain $\epsilon_{\parallel} = a(y)/a_0 - 1$ is imposed by the slight difference between the lattice parameter in the buffer and longitudinal ones in the layer. The normal strain $\epsilon_{\perp} = -D\epsilon_{\parallel}$ depends on the Poisson ratio D that determines the displacements of the atomic planes along the normal [001], [111], and [110] directions. It is to be noted that Eq. (A1) is written in the device coordinate system (DCS), whereas atomistic methods typically work in the crystal coordinate system (CCS): Figure 15 shows, for different oriented crystals, the vector basis ($e_{\parallel}^{(1)}, e_{\parallel}^{(2)}, e_{\perp}$) in which the strain tensor is expressed in its diagonal biaxial form [Eq. (A1)]. In the case of the [001]-oriented buffers, the CCS coincides with the DCS, while for the [111] buffers and [110] buffers, the strain tensor must be expressed in the CCS by means of an

appropriate rotation matrix. For the [111] buffer it can be written as¹⁵

$$\epsilon_{[111]}^{CCS} = \begin{cases} \epsilon_{xx} = \epsilon_{yy} = \epsilon_{zz} = \frac{1}{3}(\epsilon_{\perp} + 2\epsilon_{\parallel}), \\ \epsilon_{xy} = \epsilon_{xz} = \epsilon_{yz} = \frac{1}{3}(\epsilon_{\perp} - \epsilon_{\parallel}), \end{cases} \quad (\text{A2})$$

and for the [110] buffer,

$$\epsilon_{[110]}^{CCS} = \begin{cases} \epsilon_{xx} = \epsilon_{yy} = \frac{1}{2}(\epsilon_{\perp} + \epsilon_{\parallel}), \\ \epsilon_{zz} = \epsilon_{\parallel}, \\ \epsilon_{xy} = \frac{1}{2}(\epsilon_{\perp} - \epsilon_{\parallel}), \\ \epsilon_{xz} = \epsilon_{yz} = 0. \end{cases} \quad (\text{A3})$$

The shifted Bravais lattice can be determined from the strain tensor: $\mathbf{B}' = (\mathbf{I} + \epsilon^{CCS}) \cdot \mathbf{B}$. However, knowledge of the Bravais lattice is not enough to infer the position of the atoms in the unit cell. An additional degree of freedom (which occurs notably for shear distortions as it is the case in the [111]- and [110]-growth cases) must be added to the displacement of the atoms.⁶⁸ The internal strain parameter ξ , which measures how the distance between the two atoms in the unit cell changes in response to the symmetry-breaking stress, is known experimentally in Si and Ge uniaxially

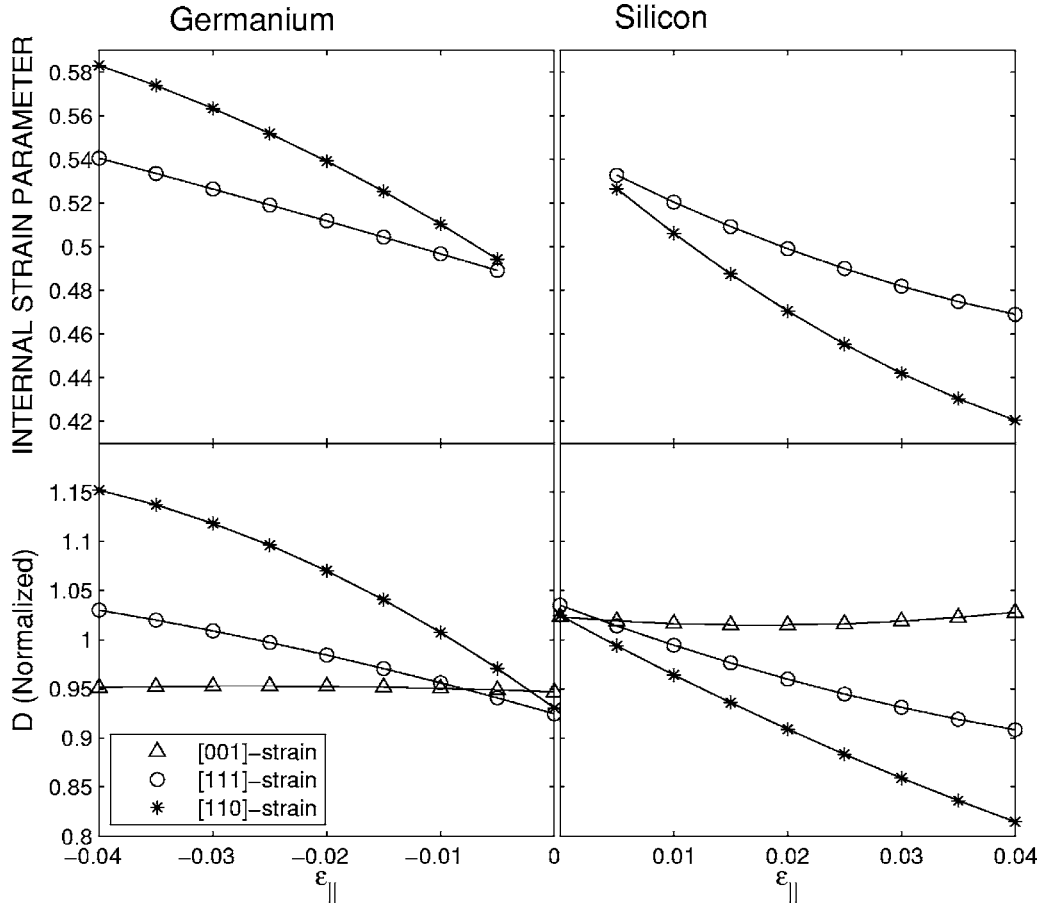


FIG. 16. Theoretical internal strain parameter ξ and theoretical normal strain coefficient D as a function of longitudinal biaxial strain applied perpendicularly to the normal [001], [111], and [110] directions. The coefficients D are normalized to the experimental values listed in Table V.

strained along the [111] direction^{69,70} (and are quoted in Table V).

In the present first-principles simulations, the internal strain parameters and the Poisson ratios have been calculated by minimizing the total energy of the biaxially strained crystal. For searching the equilibrium structure under external applied strain $\epsilon_{||}$, the total energy is minimized by varying the unit cell length along the strain direction and the atomic position in the unit cell. The theoretical Poisson ratios D_{001} , D_{111} , and D_{110} and the internal strain parameters extracted from the structural optimizations at $\epsilon_{||} \rightarrow 0$ are reported in Table V. Using continuum elasticity theory, these coefficients can be written as $D_{001} = 2(C_{12}/C_{11})$, $D_{110} = (C_{11} + 3C_{12} - 2C_{44}) / (C_{11} + C_{12} + 2C_{44})$, and $D_{111} = (2C_{11} + 4C_{12} - 4C_{44}) / (C_{11} + 2C_{12} + 4C_{44})$, where C_{11} , C_{12} , and C_{44} are the elastic constants. It can be verified in Table V that the theoretical elastic constants obtained from D_{001} , D_{111} , and D_{110} together with the above equations are in good agreement with the experimental values measured in Si and Ge.⁷¹

In Fig. 16, the theoretical Poisson ratio D and the internal strain parameter ξ are reported as a function of applied biaxial strain $\epsilon_{||}$. Simulations have been performed in tension in

Si (right) and in compression in Ge (left) for the three previously mentioned growth cases. As can be seen, for the [001]-growth case D does not significantly depend on $\epsilon_{||}$, while for the [111]- and [110]-growth cases both D and ξ change (up to $\sim 15\%$) with applied strain. The former case is consistent with results of Ref. 6 concerning strained Ge layers grown on [001]-cubic Si. Changes in ξ with applied strain have also been reported in Refs. 5, 8, and 72 as well as elastic constant strain dependence.³⁷ As shown in Sec. IV, the energy band shifts depend on the deformation applied to the crystal and thus the results shown in Fig. 16 have been carefully accounted for. For instance, we found out that the VB energy shifts in Si grown on a [111]-Ge buffer are overestimated (by roughly 10%) when both ξ and D are kept constant (this behavior is inverted in Ge grown on [111]-Si buffer).

APPENDIX B: $k \cdot p$ MATRIX FOR RELAXED MATERIALS

The 30-level $k \cdot p$ matrix [Eq. (2)] for relaxed materials can be written as

$$H_{k,p}^{30} = \begin{bmatrix} H_{\Gamma_{25^t}}^{2 \times 2} & P''' H_k^{2 \times 6} & 0 & 0 & 0 & 0 & 0 & P'' H_k^{2 \times 6} \\ & H_{\Gamma_{25^t}}^{6 \times 6} & R' H_k^{6 \times 4} & 0 & 0 & Q' H_k^{6 \times 6} & P' H_k^{6 \times 2} & H_{\Gamma_{25^t}, \Gamma_{25^t}}^{80} \\ & & H_{\Gamma_{12^t}}^{4 \times 4} & 0 & 0 & 0 & 0 & R H_k^{4 \times 6} \\ & & & H_{\Gamma_{1^u}}^{2 \times 2} & 0 & T H_k^{2 \times 6} & 0 & 0 \\ & & & & H_{\Gamma_{1^t}}^{2 \times 2} & T' H_k^{2 \times 6} & 0 & 0 \\ & & & & & H_{\Gamma_{15}}^{6 \times 6} & 0 & Q H_k^{6 \times 6} \\ & & & & & & H_{\Gamma_{2^t}}^{2 \times 2} & P H_k^{2 \times 6} \\ & & & & & & & H_{\Gamma_{25^t}}^{6 \times 6} \end{bmatrix}, \quad (\text{B1})$$

whose diagonal blocks read

$$\begin{aligned} H_{\Gamma}^{6 \times 6} &= \text{diag} \left(E_{\Gamma} + \frac{\hbar^2 k^2}{2m} \right) + H_{\Gamma}^{SO}, \\ H_{\Gamma}^{4 \times 4} &= \text{diag} \left(E_{\Gamma} + \frac{\hbar^2 k^2}{2m} \right), \\ H_{\Gamma}^{2 \times 2} &= \text{diag} \left(E_{\Gamma} + \frac{\hbar^2 k^2}{2m} \right), \end{aligned} \quad (\text{B2})$$

where $k^2 = k_x^2 + k_y^2 + k_z^2$, and $\text{diag}(\dots)$ stands for the diagonal matrix. E_{Γ} is the eigenvalue of the state labeled by Γ , as listed in Table I. The coupling constants (P, P', P'' , etc...) are listed in Table V. H_{Γ}^{SO} is the SO matrix, which depends on the SO coupling parameters listed in Table VI:

$$H_{\Gamma}^{SO} = \frac{\Delta_{\Gamma}}{3} \begin{bmatrix} -1 & -i & 0 & 0 & 0 & 1 \\ i & -1 & 0 & 0 & 0 & -i \\ 0 & 0 & -1 & -1 & i & 0 \\ 0 & 0 & -1 & -1 & i & 0 \\ 0 & 0 & -i & -i & -1 & 0 \\ 1 & i & 0 & 0 & 0 & -1 \end{bmatrix}. \quad (\text{B3})$$

The nonzero $k \cdot p$ blocks can be written as

$$H_k^{6 \times 6} = \begin{bmatrix} 0 & k_z & k_y & 0 & 0 & 0 \\ k_z & 0 & k_x & 0 & 0 & 0 \\ k_y & k_x & 0 & 0 & 0 & 0 \\ 0 & 0 & 0 & 0 & k_z & k_y \\ 0 & 0 & 0 & k_z & 0 & k_x \\ 0 & 0 & 0 & k_y & k_x & 0 \end{bmatrix},$$

$$H_k^{4 \times 6} = \begin{bmatrix} 0 & \sqrt{3}k_y & -\sqrt{3}k_z & 0 & 0 & 0 \\ 2k_x & -k_y & -k_z & 0 & 0 & 0 \\ 0 & 0 & 0 & 0 & \sqrt{3}k_y & -\sqrt{3}k_z \\ 0 & 0 & 0 & 2k_x & -k_y & -k_z \end{bmatrix},$$

$$H_k^{2 \times 6} = \begin{bmatrix} k_x & k_y & k_z & 0 & 0 & 0 \\ 0 & 0 & 0 & k_x & k_y & k_z \end{bmatrix}. \quad (\text{B4})$$

We have finally included a SO coupling term between the Γ_{25^u} and the Γ_{25^t} states and fitted the coupling strength Δ_{Γ} in order to respect the time reversal degeneracy at X .

APPENDIX C: $k \cdot p$ MATRIX FOR STRAINED MATERIALS

The perturbation matrix for strained materials [Eq. (3)] can be written as

TABLE VII. Strain perturbation matrix coefficients expressed in eV.

Symbols	Si _{1-x} Ge _x	Symbols	Si _{1-x} Ge _x	Symbols	Si _{1-x} Ge _x	Symbols	Si _{1-x} Ge _x
$l_{\Gamma_{25^t}}$	$-2.7-1.1x$	a_{12}	$7.7-0.885x$	$l_{\Gamma_{25^t}, \Gamma_{25^u}}$	$-19.8-4.339x$	$a_{\Gamma_{2^t}, \Gamma_{2^u}}$	$0.3-1.511x$
$m_{\Gamma_{25^t}}$	$4.2+0.7x$	b_{12}	$5.47+1.328x$	$m_{\Gamma_{25^t}, \Gamma_{25^u}}$	$3.9-4.024x$	$a_{\Gamma_{1^t}, \Gamma_{1^u}}$	$-2-3.927x$
$n_{\Gamma_{25^t}}$	$-7.379-2.148x$	c_{12}	$7.3+0.445x$	$n_{\Gamma_{25^t}, \Gamma_{25^u}}$	$-0.112x$	$g_{\Gamma_{12^t}, \Gamma_{2^u}}$	$-10.5+5.5x$
$l'_{\Gamma_{15}}$	$3.4+2.626x$	d_{12}	$3.65+1.208x$	$f_{\Gamma_{1^u}, \Gamma_{25^u}}$	$6+5.22x$	$g_{\Gamma_{12^t}, \Gamma_{2^t}}$	$-4.5-0.854x$
$m'_{\Gamma_{15}}$	$-0.5+1.262x$	$a_{\Gamma_{2^t}}$	$-9+1.819x$	$f_{\Gamma_{1^t}, \Gamma_{25^t}}$	$-5-2.666x$		
$n'_{\Gamma_{15}}$	$-10.392+0.258x$	$a_{\Gamma_{2^u}}$	$5-0.51x$	$f_{\Gamma_{1^u}, \Gamma_{25^t}}$	$-10-2.21x$		
$l''_{\Gamma_{25^u}}$	$-19-1.692x$	$a_{\Gamma_{1^t}}$	$10+4.171x$	$f_{\Gamma_{15}, \Gamma_{2^t}}$	$-19-3.242x$		
$m''_{\Gamma_{25^u}}$	$8+1.119x$	$a_{\Gamma_{1^u}}$	$0.5-0.992x$	$f_{\Gamma_{15}, \Gamma_{2^u}}$	$-2+21.925x$		
$n''_{\Gamma_{25^u}}$	$-1.732+2.213x$						

$$W_{k-p}^{30} = \begin{bmatrix} W_{\Gamma_{2'iu}}^{2 \times 2} & P''' W_k^{2 \times 6} & W_{\Gamma_{2'iu}, \Gamma_{12'}}^{2 \times 4} & 0 & 0 & W_{\Gamma_{2'iu}, \Gamma_{15}}^{2 \times 6} & W_{\Gamma_{2'iu}, \Gamma_{2'it}}^{2 \times 2} & P'' W_k^{2 \times 6} \\ & W_{\Gamma_{25'iu}}^{6 \times 6} & R' W_k^{6 \times 4} & W_{\Gamma_{25'iu}, \Gamma_{1u}}^{6 \times 2} & W_{\Gamma_{25'iu}, \Gamma_{1t}}^{6 \times 2} & Q' W_k^{6 \times 6} & P' W_k^{6 \times 2} & W_{\Gamma_{25'it}, \Gamma_{25'iu}}^{6 \times 6} \\ & & W_{\Gamma_{12'}}^{4 \times 4} & 0 & 0 & W_{\Gamma_{12'}, \Gamma_{15}}^{4 \times 6} & W_{\Gamma_{12'}, \Gamma_{2'it}}^{4 \times 2} & R W_k^{4 \times 6} \\ & & & W_{\Gamma_{1u}}^{2 \times 2} & W_{\Gamma_{1u}, \Gamma_{1t}}^{2 \times 2} & T W_k^{2 \times 6} & 0 & W_{\Gamma_{1u}, \Gamma_{25'it}}^{2 \times 6} \\ & & & & W_{\Gamma_{1t}}^{2 \times 2} & T' W_k^{2 \times 6} & 0 & W_{\Gamma_{1t}, \Gamma_{25'it}}^{2 \times 6} \\ & & & & & W_{\Gamma_{15}}^{6 \times 6} & W_{\Gamma_{15}, \Gamma_{2'it}}^{6 \times 2} & Q W_k^{6 \times 6} \\ & & & & & & W_{\Gamma_{2'it}}^{2 \times 2} & P W_k^{2 \times 6} \\ & & & & & & & W_{\Gamma_{25'it}}^{6 \times 6} \end{bmatrix}. \quad (\text{C1})$$

There are two types of coupling terms in the matrix described by Eq. (C1); k -independent terms (labeled W_{Γ}) coming from the second term in Eq. (3) and terms that are linear in k (labeled W_k) coming from the first term in Eq. (3).

The k -independent W_{Γ} blocks can be written as

$$W_{\Gamma}^{6 \times 6} = \begin{bmatrix} W_{\Gamma}^{3 \times 3} & 0 \\ 0 & W_{\Gamma}^{3 \times 3} \end{bmatrix},$$

$$W_{\Gamma}^{3 \times 3} = \begin{bmatrix} l\epsilon_{xx} + m(\epsilon_{yy} + \epsilon_{zz}) & n\epsilon_{xy} & n\epsilon_{xz} \\ n\epsilon_{xy} & l\epsilon_{yy} + m(\epsilon_{xx} + \epsilon_{zz}) & n\epsilon_{yz} \\ n\epsilon_{xz} & n\epsilon_{yz} & l\epsilon_{zz} + m(\epsilon_{xx} + \epsilon_{yy}) \end{bmatrix},$$

$$W_{\Gamma_{12}}^{4 \times 4} = \begin{bmatrix} A\epsilon_{xx} + B(\epsilon_{yy} + \epsilon_{zz}) & E(\epsilon_{yy} - \epsilon_{zz}) & 0 & 0 \\ E(\epsilon_{yy} - \epsilon_{zz}) & C\epsilon_{xx} + D(\epsilon_{yy} + \epsilon_{zz}) & 0 & 0 \\ 0 & 0 & A\epsilon_{xx} + B(\epsilon_{yy} + \epsilon_{zz}) & E(\epsilon_{yy} - \epsilon_{zz}) \\ 0 & 0 & E(\epsilon_{yy} - \epsilon_{zz}) & C\epsilon_{xx} + D(\epsilon_{yy} + \epsilon_{zz}) \end{bmatrix},$$

$$W_{\Gamma}^{2 \times 2} = a_{\Gamma} \sum_i \begin{bmatrix} \epsilon_{ii} & 0 \\ 0 & \epsilon_{ii} \end{bmatrix},$$

$$W_{\Gamma}^{2 \times 6} = f_{\Gamma} \begin{bmatrix} \epsilon_{yz} & \epsilon_{xz} & \epsilon_{xy} & 0 & 0 & 0 \\ 0 & 0 & 0 & \epsilon_{yz} & \epsilon_{xz} & \epsilon_{xy} \end{bmatrix},$$

$$W_{\Gamma}^{4 \times 2} = g_{\Gamma} \begin{bmatrix} \sqrt{3}(\epsilon_{yy} - \epsilon_{zz}) & 0 \\ 2\epsilon_{xx} - \epsilon_{yy} - \epsilon_{zz} & 0 \\ 0 & \sqrt{3}(\epsilon_{yy} - \epsilon_{zz}) \\ 0 & 2\epsilon_{xx} - \epsilon_{yy} - \epsilon_{zz} \end{bmatrix},$$

$$W_{\Gamma}^{4 \times 6} = h_{\Gamma} \begin{bmatrix} 0 & \sqrt{3}\epsilon_{xz} & -\sqrt{3}\epsilon_{xy} & 0 & 0 & 0 \\ 2\epsilon_{yz} & -\epsilon_{xz} & -\epsilon_{xy} & 0 & 0 & 0 \\ 0 & 0 & 0 & 0 & \sqrt{3}\epsilon_{xz} & -\sqrt{3}\epsilon_{xy} \\ 0 & 0 & 0 & 2\epsilon_{yz} & -\epsilon_{xz} & -\epsilon_{xy} \end{bmatrix}. \quad (\text{C2})$$

The deformation potentials (l, n, m , etc.) are listed in Table VII (the coefficients not mentioned in the table are set to zero). Group-theory considerations allow us to write the five coefficients A , B , C , D , and E as a linear combination of four coefficients:

$$A = 6(b_{12} - d_{12}),$$

$$B = 3(a_{12} + b_{12} - 2c_{12}),$$

$$C = 2(2a_{12} - 4c_{12} + b_{12} + d_{12}),$$

$$D = 5b_{12} - 2c_{12} - 4d_{12} + a_{12},$$

$$E = \sqrt{3}(2c_{12} - 2d_{12} - a_{12} + b_{12}). \quad (\text{C3})$$

The first term in Eq. (3) gives rise to an additional nondiagonal k -independent coupling between states of the same polarity. These blocks and the corresponding deformation potentials have been labeled using a double-subscript notation (e.g., $W_{\Gamma_{12},\Gamma_{2''}}$). For simplicity, we dropped the double-subscript notation for the coupling between identical states (e.g., $W_{\Gamma_{12}}$).

Finally, the $\mathbf{k} \cdot \mathbf{p}$ coupling terms due to the second term in Eq. (3) can be written as

$$W_k^{6 \times 6} = - \sum_i \begin{bmatrix} 0 & \epsilon_{iz}k_i & \epsilon_{yi}k_i & 0 & 0 & 0 \\ \epsilon_{iz}k_i & 0 & \epsilon_{xi}k_i & 0 & 0 & 0 \\ \epsilon_{iy}k_i & \epsilon_{ix}k_i & 0 & 0 & 0 & 0 \\ 0 & 0 & 0 & 0 & \epsilon_{iz}k_i & \epsilon_{yi}k_i \\ 0 & 0 & 0 & \epsilon_{iz}k_i & 0 & \epsilon_{xi}k_i \\ 0 & 0 & 0 & \epsilon_{iy}k_i & \epsilon_{ix}k_i & 0 \end{bmatrix},$$

$$W_k^{4 \times 6} = - \sum_i \begin{bmatrix} 0 & \sqrt{3}\epsilon_{iy}k_i & -\sqrt{3}\epsilon_{iz}k_i & 0 & 0 & 0 \\ 2\epsilon_{ix}k_i & -\epsilon_{iy}k_i & -\epsilon_{iz}k_i & 0 & 0 & 0 \\ 0 & 0 & 0 & 0 & \sqrt{3}\epsilon_{iy}k_i & -\sqrt{3}\epsilon_{iz}k_i \\ 0 & 0 & 0 & 2\epsilon_{ix}k_i & -\epsilon_{iy}k_i & -\epsilon_{iz}k_i \end{bmatrix},$$

$$W_k^{2 \times 6} = - \sum_i \begin{bmatrix} \epsilon_{ix}k_i & \epsilon_{iy}k_i & \epsilon_{iz}k_i & 0 & 0 & 0 \\ 0 & 0 & 0 & \epsilon_{ix}k_i & \epsilon_{iy}k_i & \epsilon_{iz}k_i \end{bmatrix}, \quad (\text{C4})$$

where i stands for x , y , and z .

*Electronic address: denis.rideau@st.com

†Also at Physics Department, INSA Lyon, France.

¹F. Schaffler, *Semicond. Sci. Technol.* **12**, 1515 (1997).

²C. K. Maiti, L. K. Bera, and S. Chattopadhyay, *Semicond. Sci. Technol.* **13**, 1225 (1998).

³R. J. H. Morris, T. J. Grasby, R. Hammond, M. Myronov, O. A. Mironov, D. R. Leadley, T. E. Whall, E. H. C. Parker, M. T. Currie, C. W. Leitz, and E. A. Fitzgerald, *Semicond. Sci. Technol.* **19**, L106 (2004).

⁴M. C. Payne, M. P. Teter, D. C. Allan, T. A. Arias, and J. D. Joannopoulos, *Rev. Mod. Phys.* **64**, 1045 (1992).

⁵O. H. Nielsen and R. M. Martin, *Phys. Rev. B* **32**, 3780 (1985); **32**, 3792 (1985).

⁶C. G. Van de Walle and R. M. Martin, *Phys. Rev. B* **34**, 5621 (1986).

⁷C. G. Van de Walle, *Phys. Rev. B* **39**, 1871 (1989).

⁸Z. H. Levine, J. H. Burnett, and E. L. Shirley, *Phys. Rev. B* **68**, 155120 (2003).

⁹L. Hedin, *Phys. Rev.* **139**, A796 (1965).

¹⁰J. R. Chelikowsky and M. L. Cohen, *Phys. Rev. B* **14**, 556 (1976).

¹¹M. A. Gell, *Phys. Rev. B* **38**, 7535 (1988); M. Gell, *ibid.* **41**, 7611 (1990).

¹²P. Friedel, M. S. Hybertsen, and M. Schluter, *Phys. Rev. B* **39**, 7974 (1989).

¹³J. M. Fischetti and S. E. Laux, *J. Appl. Phys.* **80**, 2234 (1996).

¹⁴M. M. Rieger and P. Vogl, *Phys. Rev. B* **48**, 14276 (1993).

¹⁵Q. M. Ma, K. L. Wang, and J. N. Schulman, *Phys. Rev. B* **47**, 1936 (1993).

¹⁶C. Tserbak, H. M. Polatoglou, and G. Theodorou, *Phys. Rev. B* **47**, 7104 (1993); C. Tserbak and G. Theodorou, *ibid.* **52**, 12232 (1995).

¹⁷G. Dresselhaus, A. F. Kip, and C. Kittel, *Phys. Rev.* **98**, 368 (1955).

¹⁸M. Elkurdi, G. Fishman, S. Sauvage, and P. Boucaud, *Phys. Rev. B* **68**, 165333 (2003).

¹⁹M. Cardona and F. Pollak, *Phys. Rev.* **142**, 530 (1966).

²⁰F. Pollak, M. Cardona, and C. W. Higginbotham, *Phys. Rev. B* **2**, 352 (1970).

²¹S. Richard, F. Aniel, and G. Fishman, *Phys. Rev. B* **70**, 235204 (2004); **71**, 169901(E) (2005).

²²R. G. Humphreys, *J. Phys. C* **14**, 2935 (1981).

²³E. Pikus and G. L. Bir, *Fiz. Tverd. Tela (Leningrad)* **1**, 1642 (1959) [*Sov. Phys. Solid State* **1**, 1502 (1960)].

²⁴All DFT-LDA simulations were performed using the ABINIT v4.6.5 package (<http://www.abinit.org>).

²⁵C. Hartwigsen, S. Goedecker, and J. Hutter, *Phys. Rev. B* **58**, 3641 (1998).

²⁶D. M. Ceperley and B. J. Alder, *Phys. Rev. Lett.* **45**, 566 (1980).

²⁷V. Fiorentini, *Phys. Rev. B* **46**, 2086 (1992).

²⁸*Physics of Group IV Elements and III-V Compounds*, edited by O. Madelung, Landolt-Bornstein: Numerical Data and Functional Relationships in Science and Technology, Group III (Springer-

- Verlag, Berlin, 1982), Vol. 17a.
- ²⁹W. G. Aulbur, L. Jonsson, and J. W. Wilkins, *Solid State Phys.* **54**, 1 (2000).
- ³⁰M. S. Hybertsen and S. G. Louie, *Phys. Rev. Lett.* **55**, 1418 (1985).
- ³¹M. Rohlfing, P. Kruger, and J. Pollmann, *Phys. Rev. B* **48**, 17791 (1993); *Phys. Rev. B* **52**, 1905 (1995).
- ³²In the present paper, in order to distinguish the corrected *GW* data from the original G_0W_0 results, the subscripts are dropped out whenever the correction is applied.
- ³³S. Wei, D. C. Allan, and J. W. Wilkins, *Phys. Rev. B* **46**, 12411 (1992).
- ³⁴H. J. Monkhorst and J. D. Pack, *Phys. Rev. B* **13**, 5188 (1976).
- ³⁵M. L. Tiago, S. Ismail-Beigi, and S. G. Louie, *Phys. Rev. B* **69**, 125212 (2004).
- ³⁶J. P. Dismukes, L. Ekstrom, and R. J. Paff, *J. Phys. Chem.* **68**, 3021 (1964).
- ³⁷Y. Umeno and T. Kitamura, *Mater. Sci. Eng., B* **88**, 79 (2002).
- ³⁸X. Zhu, S. Fahy, and S. G. Louie, *Phys. Rev. B* **39**, 7840 (1989).
- ³⁹J. E. Ortega and F. J. Himpsel, *Phys. Rev. B* **47**, 2130 (1993).
- ⁴⁰P. Lautenschlager, M. Garriga, L. Vina, and M. Cardona, *Phys. Rev. B* **36**, 4821 (1987).
- ⁴¹L. Viña, S. Logothetidis, and M. Cardona, *Phys. Rev. B* **30**, 1979 (1984).
- ⁴²M. S. Hybertsen and S. G. Louie, *Phys. Rev. B* **34**, 5390 (1986).
- ⁴³L. P. Bouckaert, R. Smoluchowski, and E. Wigner, *Phys. Rev.* **50**, 58 (1936).
- ⁴⁴N. Cavassilas, F. Aniel, K. Boujdaria, and G. Fishman, *Phys. Rev. B* **64**, 115207 (2001).
- ⁴⁵For the purpose of obtaining a continuous description of K and U , as required, for instance, in MC simulators (Ref. 57), we found a satisfactory solution using a smoothing function on the P''' parameter, reducing locally (in the near- K region) its value to 1.3 a.u. All figures shown in this work have been obtained with this smoothing function.
- ⁴⁶The present $\mathbf{k}\cdot\mathbf{p}$ matrix uses for Γ_{12} the functions γ_{1-} and γ_{2-} as in Ref. 17, while Cardona and Pollak (Ref. 19) use $\frac{1}{2}(\gamma_{1-} - \gamma_{2-})$ and $\frac{1}{2}(\gamma_{1-} + \gamma_{2-})$. The coefficients R and R' are $\frac{1}{\sqrt{2}}$ smaller in this work.
- ⁴⁷As written in Eq. (2), the $\mathbf{k}\cdot\mathbf{p}$ Hamiltonian does not explicitly include nonlocal corrections to the purely local operator $V(r)$. In this work, the nonlocal effects have been “renormalized” into the $\mathbf{k}\cdot\mathbf{p}$ parameters. In Ge where these effects are prominent (Ref. 10), certain coefficients (e.g., $P=1.186$ a.u.) are smaller than Cardona and Pollak’s (Ref. 19) ones (e.g., $P=1.36$ a.u.).
- ⁴⁸U. Schmid, N. E. Christensen, and M. Cardona, *Phys. Rev. B* **41**, 5919 (1990).
- ⁴⁹C. Kittel, *Quantum Theory of Solids*, 2nd revised ed. (Wiley, New York, 1987).
- ⁵⁰The present EPM simulations in strained material are based on the method shown in Ref. 13. However, in order to improve the accuracy of the deformation potentials and energy band shifts with experimental data, we used a slightly different form-factors interpolation function.
- ⁵¹D. E. Aspnes and M. Cardona, *Phys. Rev. B* **17**, 726 (1978).
- ⁵²P. Lawaetz, *Phys. Rev. B* **4**, 3460 (1971).
- ⁵³O. A. Makarov, N. N. Ovsyuk, and M. P. Sinyukov, *Sov. Phys. JETP* **57**, 1318 (1983).
- ⁵⁴B. W. Levinger and D. R. Frankl, *J. Phys. Chem. Solids* **18**, 139 (1961).
- ⁵⁵J. Halpern and B. Lax, *J. Phys. Chem. Solids* **26**, 911 (1965).
- ⁵⁶P. Fantini, A. Ghetti, G. P. Carnavale, E. Bonera, and D. Rideau, *IEDM Tech. Dig.* **2005**, 1013.
- ⁵⁷M. Feraille, D. Rideau, A. Ghetti, A. Poncet, C. Tavernier, and H. Jaouen, in *Proc. SISPAD Conference* (IEEE Electron Devices Society, 2006), p. 264; A. Ghetti and D. Rideau, in *Proc. SISPAD Conference* (IEEE Electron Devices Society, 2006), p. 67.
- ⁵⁸G. Gilat and L. J. Raubenheimer, *Phys. Rev.* **144**, 390 (1966).
- ⁵⁹M. Chandrasekhar and F. H. Pollak, *Phys. Rev. B* **15**, 2127 (1977).
- ⁶⁰G. S. Cargill, III, J. Angilello, and K. L. Kavanagh, *Phys. Rev. Lett.* **61**, 1748 (1988).
- ⁶¹D. D. Nolte, W. Walukiewicz, and E. E. Haller, *Phys. Rev. Lett.* **59**, 501 (1987).
- ⁶²Y. H. Li, X. G. Gong, and S. H. Wei, *Phys. Rev. B* **73**, 245206 (2006).
- ⁶³G. Schubert, F. Schaffler, M. Besson, G. Abstreiter, and E. Gornik, *Appl. Phys. Lett.* **59**, 3318 (1991).
- ⁶⁴J. C. Hensel and G. Feher, *Phys. Rev.* **129**, 1041 (1963).
- ⁶⁵H. Irie, K. Kita, K. Kyuno, and A. Toriumi, *IEDM Tech. Dig.* **2004**, 225.
- ⁶⁶In general, for the EPM, it is necessary to use a set of 100–200 plane waves. On the contrary, a set of only 30 Γ -centered Bloch functions is sufficient in the $\mathbf{k}\cdot\mathbf{p}$ method. This leads to a substantial difference in terms of computation time. Moreover, in the relativistic nonlocal EPM (Ref. 10) a significant computation effort is spent evaluating transcendental functions (e.g., Bessel functions) while in the $\mathbf{k}\cdot\mathbf{p}$ Hamiltonian only algebraic terms linear in k are calculated.
- ⁶⁷S. Richard, F. Aniel, G. Fishman, and N. Cavassilas, *J. Appl. Phys.* **94**, 1795 (2003).
- ⁶⁸L. Kleinman, *Phys. Rev.* **128**, 2614 (1962); **130**, 2283 (1963); I. Goroff and L. Kleinman, *ibid.* **132**, 1080 (1963).
- ⁶⁹Experimental values for $\xi \in [0,1]$. However, as pointed out by Levine *et al.* (Ref. 8) most of the theoretical internal strain parameter calculations (Refs. 5 and 33) have used a nonstandard definition of ξ (i.e., $\xi' = \frac{2}{3}\xi$) which implies $\xi' \in [0, \frac{2}{3}]$. In this text we used ξ' , and for simplicity the prime is dropped in the notations.
- ⁷⁰C. S. G. Cousins, *et al.*, *J. Phys. C* **20**, 29 (1987).
- ⁷¹H. J. McKimiu, *J. Appl. Phys.* **24**, 988 (1953), cited by Ref. 7.
- ⁷²J. Sanchez-Dehesa, C. Tejedor, and J. A. Verges, *Phys. Rev. B* **26**, 5960 (1982).